



# Immobilization of U(VI) onto covalent organic frameworks with the different periodic structure by photocatalytic reduction

Xin Zhong<sup>\*</sup>, Qian Ling, Zhenyu Ren, Baowei Hu<sup>\*</sup>

School of Life and Environmental Sciences, Shaoxing University, Huanheng West Road 508, Shaoxing 312000, PR China

## ARTICLE INFO

### Keywords:

COFs  
U(VI) adsorption  
U(VI) photoreduction

## ABSTRACT

In recent years, the donor (D)-acceptor (A) covalent organic frameworks (COFs) have attracted more and more attention in photocatalysis, but the photoinduced electron-transfer in the COFs have not been revealed. Herein, three 2D COFs materials (Tp-Tapb, Tp-Taz and TpTt, among them, Tp= 1,3,5-Triformylphloroglucinol, Tapb=1,3,5-tris(4-aminophenyl)-benzene, Tt=melamine, Taz= 4,4',4''-(1,3,5-triazine-2,4,6-triyl)-trianiline) with similar structure, different building monomers with number acceptors and the distance between the two acceptors were synthesized. COFs were considered as potential adsorbents to capture uranium (U(VI)) from wastewater due to high specific surface area, stability and heteroatom content. Compared with Tp-Tapb, Tp-Taz and TpTt shown the better photocatalytic performance and the higher separation efficiency of  $e^-$ - $h^+$ , due to the coexistence of triazine and ketone groups. Furthermore, TpTt possessed two short-range acceptor units (triazine and ketone) with the high content of heteroatoms, which exhibited the highest adsorption (505 mg/g) and photoreduction ( $0.22\text{ h}^{-1}$ ) performances. The photocatalytic reduction of U(VI) by these three COFs materials, U(VI) was photo-reduced by  $e^-$  and  $\bullet\text{O}_2$  in the frameworks of photoactive COFs under visible-light irradiation, so then the insoluble U(IV) species ( $\text{UO}_2$ ,  $\text{UO}_{2.9}$ ,  $\text{UO}_{2.87}$ ,  $\text{UO}_{2.82}$ ) were deposited in the open channels. COFs served as the composite platform with high catalytic activity and chelating coordination ability. The mutual enhancement of adsorption and photogenerated electron-transfer can realize the efficient removal of U(VI).

## 1. Introduction

Uranium is a significant strategic resource, but its reserves are limited [1,2]. Uranium in nuclear waste liquids has chemical toxicity and radiotoxicity, which is harmful to human health and ecological environment [3,4]. Therefore, efficient removal of uranium pollution and recovery of uranium resources are of great significance to the sustainable development of nuclear industry and environment [5]. Adsorption is an effective method to remove and extract uranium from wastewater [6–8]. Interestingly, uranium (U) is a redox-active metal in which highly soluble uranyl ion (U(VI)) can be reduced to insoluble U(IV) in multiple ways [9–11]. Thus, semiconductor-based photocatalytic reduction of U(VI) provides an enhanced method for removing U(VI) from wastewater, such as  $\text{MoS}_2$  [12],  $\text{g-C}_3\text{N}_4$  [13],  $\text{TiO}_2$  [14],  $\text{CuS}$  [15],  $\text{WO}_3$  [16]. However, the adsorption capacities of these semiconductor materials for U(VI) were quite limited, because these photocatalysts cannot preconcentrate U(VI) from solution in advance.

Covalent organic frameworks (COFs) are composed of the ordered organic molecular construction units by covalent bonds, which have

unprecedented structural design, crystallinity and porosity [17]. Crystalline porous COFs material has great potential in U extraction and wastewater purification due to its periodic structure, high surface area, adjustable pore size, abundant coordination sites, chemical and thermal stability, as well as high radiation resistance [18,19]. Besides, 2D COFs structures have  $\pi$ -conjugate structure in the plane and discontinuous  $\pi$ -electron delocalization throughout frameworks [20–22]. Due to efficient charge and energy transfer, these materials have been studied in many fields, such as photovoltaics [23], sensors [24] and heterogeneous catalysis [25–27]. In 2D COF-based semiconductor, the extensive light absorption in the visible region, the appropriate band gap energy, and the high photogenerated excitons separation are the decisive characteristics to ensure the photocatalytic activity of COFs, which depends on the chemical composition, the size of the conjugated structure and the polarity of adjacent units [28–31]. The structure and properties of COFs can be controlled at the atomic level due to its wide range of organic building blocks, flexible connections, diverse topological types and structural designability. Therefore, the optical properties and photocatalytic properties of COFs could be adjusted by changing the monomer

<sup>\*</sup> Corresponding authors.

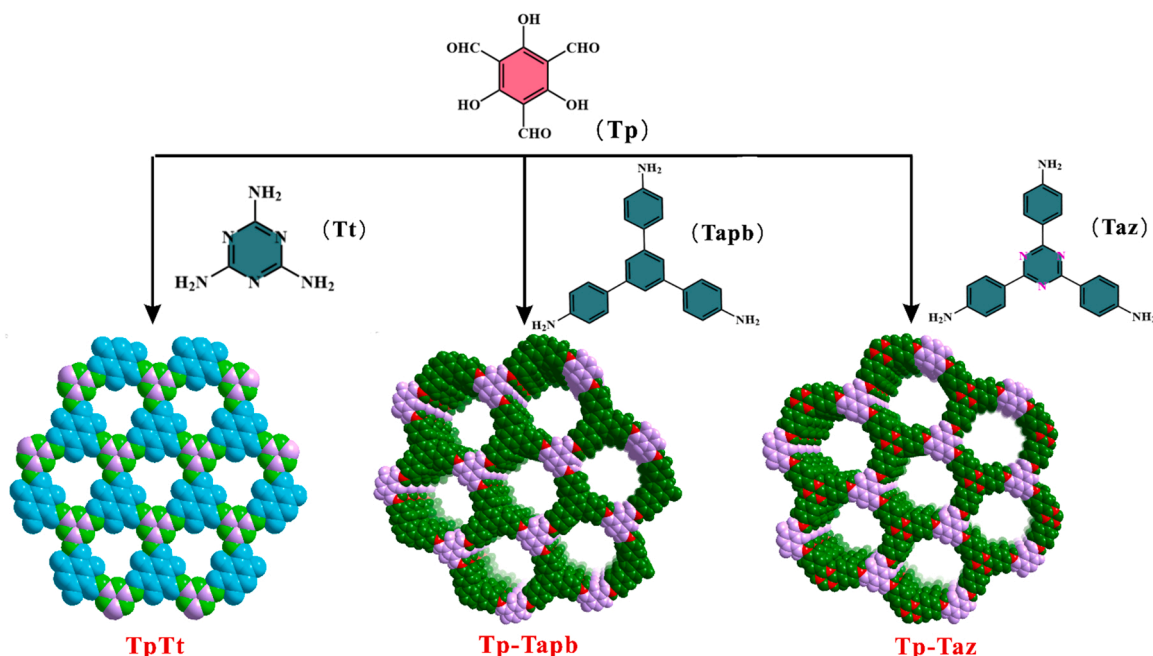
E-mail addresses: [zhongxinmagic@163.com](mailto:zhongxinmagic@163.com) (X. Zhong), [hbw@usx.edu.cn](mailto:hbw@usx.edu.cn) (B. Hu).

<https://doi.org/10.1016/j.apcatb.2023.122398>

Received 20 September 2022; Received in revised form 27 December 2022; Accepted 10 January 2023

Available online 11 January 2023

0926-3373/© 2023 Elsevier B.V. All rights reserved.



**Scheme 1.** The synthetic illustration of Tp-Tapb, Tp-Taz and TpTt.

or monomer modification. However, so far, only a few studies have evaluated adjusting the band gap of 2D COFs to achieve visible-light driven photocatalytic reaction, so it is urgent to clarify the structure-property relationship of COFs [32–36]. Therefore, in order to improve the light utilization, one strategy is to adjust the conjugate structure, although potentially inappropriate chain penetration would have a negative impact on the pores of COFs [37]. In addition, the introduction of donor-acceptor (D-A) groups containing heteroatoms into the COFs structure could promote charge separation and conversion [38–40].

In this work, three COFs were constructed by the Schiff-base reaction to scrutinize the different number acceptors, and the influence of the distance between the two acceptors on the electron-hole separation though altering the length of bridged benzene ring. Specially, 1,3,5-Triformylphloroglucinol (Tp) were separately condensed with 1,3,5-tris(4-aminophenyl)-benzene (Tapb) and 4,4',4''-(1,3,5-triazine-2,4,6-triyl)-trianiline (Taz) to obtain COFs named Tp-Tapb (where had one acceptor, ketone) and Tp-Taz (where had two acceptors, triazine and ketone). Additionally, melamine (Tt) reacted with Tp to produce COF-TpTt, and the distance between the two acceptors was shortened compared with the above synthesized Tp-Taz. More than that, triazine ligands (Taz and Tt) contained abundant nitrogen atoms, which was a good electron acceptor. Furthermore, we investigated the photocatalytic reduction of U(VI) by these three COFs materials, U(VI) was photo-reduced by electrons from the photoactive COFs frameworks under visible-light irradiation, so that insoluble U(IV) species were stored in the open channels. Finally, we compared their photoelectric properties owing to discussed the mechanism of photocatalytic reduction and revealed structure-activity relationship.

## 2. Chemicals and methods

### 2.1. Chemicals and characterization

All the chemical reagents used were analytical grade without further purification. 1, 3, 5-tris(4-aminophenyl)-benzene (Tapb,  $\geq 97\%$ ), melamine (Tt,  $\geq 95\%$ ), 4, 4', 4''-(1,3,5-triazine-2,4,6-triyl)-trianiline (Taz,  $\geq 95\%$ ), Arsenazo III,  $\text{UO}_2(\text{NO}_3)_2 \cdot 6 \text{H}_2\text{O}$  and the other chemical reagents were purchased from Macklin Bio-chemical Co., Ltd (Shanghai, China).

1, 3, 5-Triformylphloroglucinol (Tp,  $\geq 97\%$ ) was obtained from Yanshen Technology Co., Ltd. (Jilin, China). All the chemicals and solvents were used directly without further purification. The detailed characterizations of the prepared COFs were shown in Electronic Supporting Information (ESI).

### 2.2. Preparation methods

Tp-Tapb, Tp-Taz and TpTt were synthesized by appropriate adjustment according to the previously reported methods [41–43]. In detail, 63 mg of Tp (0.3 mmol) and 38 mg of Tt (0.3 mmol) were dissolved in *N,N*-dimethylacetamide (DMAc), dimethyl sulfoxide (DMSO) and 6 M acetic acid (DMAc/DMSO/AcOH=2 mL/1 mL/0.3 mL), kept at 120 °C for 72 h and obtained TpTt. 10.5 mg of Tp (0.05 mmol) and 17.7 mg of Taz (0.05 mmol) were dispersed in dioxane and 3 M acetic acid (dioxane/AcOH=1 mL/0.2 mL) under 120 °C for 72 h, acquiring Tp-Taz. Similarly, 10.5 mg of Tp (0.05 mmol) and 17.6 mg of Tapb (0.05 mmol) were added into *o*-dichlorobenzene (*o*-DCB), *n*-butyl alcohol (*n*-BuOH) and 3 M acetic acid (*o*-DCB/ *n*-BuOH/AcOH=0.5 mL/0.5 mL/0.1 mL), reacted at 120 °C for 72 h, getting Tp-Tapb. The synthesis processes and structures of three COFs material were shown in Scheme 1.

### 2.3. Batch adsorption experiments

The U(VI) capture capacity experiments were carried out by using 2.0 mg COFs materials into 100 mL ( $C_0 = 0 \sim 100$  ppm) U(VI) solution. The pH value of the system was adjusted to 2.0–8.0 by adding small amount of NaOH and  $\text{HNO}_3$  solutions. Afterwards, under the dark condition of 25 ~ 45 °C, the suspensions were stirred for different times. Regularly took out of solution with 0.22  $\mu\text{m}$  membrane filter filtration, and the filtrate was collected and measured by using Arsenazo-III spectrophotometric method ( $\lambda = 650$  nm) to obtain the remaining concentration of U(VI). The adsorption capacity ( $q_b$ , mg/g) was figured out by using Eq. (1). Where,  $m$  (g) was COF material dosage and  $V$  (L) was the solution volume.  $C_0$  (mg/L) and  $C_t$  (mg/L) were the initial concentration and the concentration for a certain time ( $t$ ), respectively. Besides, 0.1 mol/L  $\text{HNO}_3$  was used as the eluent for the cyclic adsorption-desorption experiments.

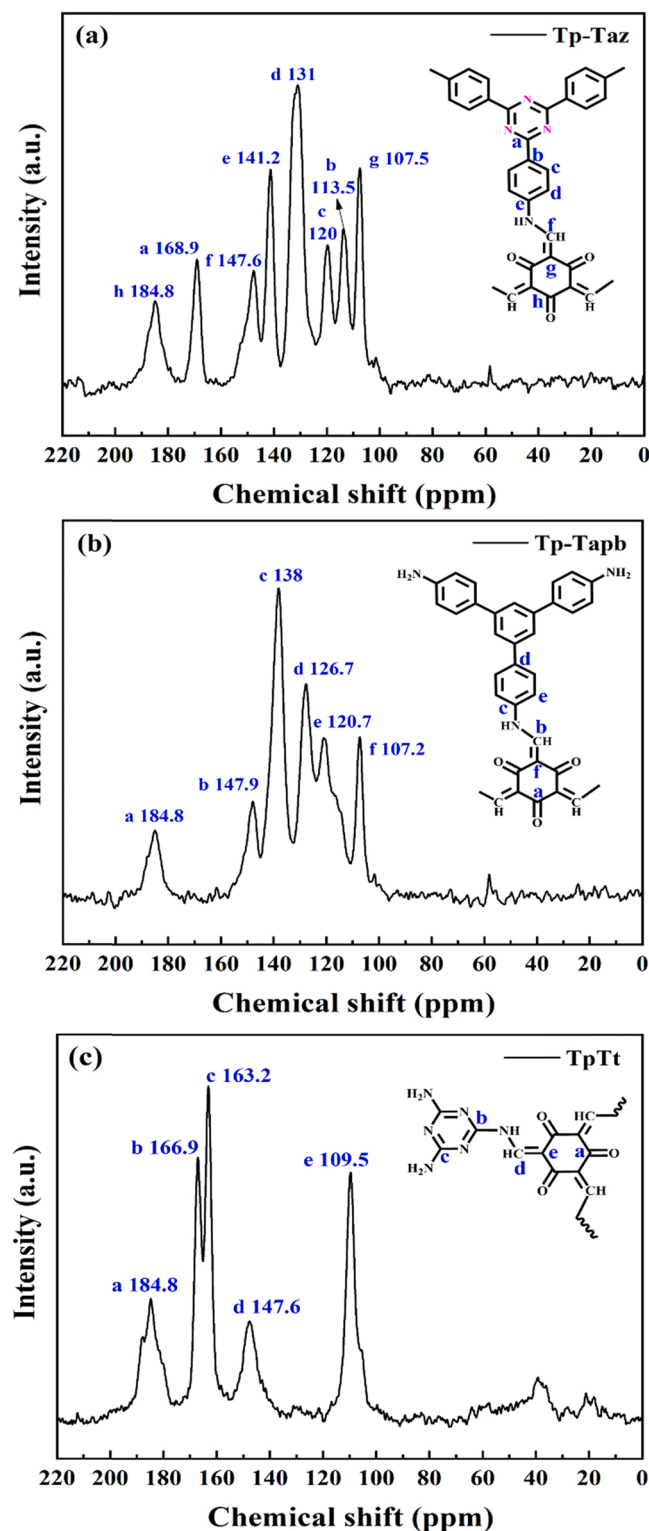


Fig. 1. Solid-state  $^{13}\text{C}$  CP-MAS NMR spectra of (a) Tp-Taz, (b) Tp-Tapb and (c) TpTt.

$$qt = \frac{C_0 - C_t}{m} \times V \quad (1)$$

#### 2.4. Photocatalytic reduction of U(VI)

The photocatalytic properties of Tp-Taz, Tp-Tapb, TpTt samples were evaluated by U(VI) adsorption and photoreduction. The three COFs

materials (8.0 mg) were left for 60 min to establish absorption-desorption equilibrium of 30 ppm U(VI) solution (35 mL) under the dark condition, and used a 500 W xenon lamp (with a cut-off filter,  $\lambda > 420$  nm) to irradiate the reaction solution. Regularly took out 1 mL of solution to measure the residual concentration of U(VI).

$$\text{Removal Efficiency (R)}\% = \frac{(C_0 - C_t)}{C_0} \times 100\% \quad (2)$$

### 3. Results and discussion

#### 3.1. Textural characterizations

As shown in XRD patterns (Fig. S1a-c), Tp-Taz had a long-range ordered structure with peaks at  $2\theta = 5.6^\circ$ ,  $9.8^\circ$  and  $25^\circ$ , which were attributed to the (100), (110) and (001) inflection, respectively [34]. Besides, the strong peak on the (001) plane indicated the strong  $\pi$ - $\pi$  stacking. TpTt displayed two characteristic peaks at  $2\theta = 9.7^\circ$  and  $27.4^\circ$ , corresponding to the reflections of the (100) and (002) planes, respectively [44]. Tp-Tapb showed two peaks at  $2\theta = 5.6^\circ$  and  $9.7^\circ$  belonged to (100) and (011) planes, respectively [45]. For FT-IR patterns of Tp-Taz, TpTt and Tp-Tapb (Fig. S1d-e), the peak at  $\sim 1620$   $\text{cm}^{-1}$  was assigned to stretching frequency of C=O, which appeared as a result of enol to keto tautomerism. The strong peak at  $1574$   $\text{cm}^{-1}$  can be assigned to C=C bond, and the peak at  $\sim 1247$   $\text{cm}^{-1}$  was observed because of the newly formed C-N bond of the Tp-Taz, Tp-Tapb, TpTt framework [42,45,46].

Additionally, the bonding state was further confirmed by  $^{13}\text{C}$  NMR spectra (Fig. 1). The spectra of Tp-Taz, Tp-Tapb and TpTt displayed the characteristic signal at 184.8 ppm assignable to the C=O carbon, ascribing to the enol-keto tautomerism into the stable COFs [42,45,47]. Tp-Taz (Fig. 1a) exhibited the peaks at 168.9, 147.6 and 107.5 ppm, assigning to the triazine carbons (N-C=N), C-N and C=C bonds, respectively [48]. Similarly, the signals of Tp-Tapb at 147.6 and 107.5 ppm belong to C-N and C=C bonds (Fig. 1b). TpTt showed the doublet peaks at 166.9 and 163.2 ppm for aromatic carbons of the triazine unit (Fig. 1c) [42]. Besides, the rest of the peaks located at the range of 100–140 ppm corresponded to the highly conjugated phenyl framework [49].

To further verify the chemical compositions of Tp-Taz, Tp-Tapb, TpTt, XPS analysis (Fig. S2) and elemental analysis (Table S1) were investigated. As shown in Fig. S2a, the full XPS spectra all had three peaks with binding energies of  $\sim 285$  eV,  $\sim 399$  eV and  $\sim 532$  eV, corresponding to C 1s, N 1s and O 1s, respectively. For TpTt, the high-resolution C 1s spectrum (Fig. S2b) could be deconvoluted into four peaks with binding energies of 284.7, 286.5, 288.1 and 290.3 eV, represented carbon atoms in the triazine ring (C-N, C=N) and linkage ( $\text{sp}^2$  C=C, C=O) [46]. The spectrum of N 1s (Fig. S2d) can be resolved into the triazine groups (C-N=C) at 398.8 eV and the -N-H groups at 400.1 eV, respectively [50]. The O1s spectrum (Fig. S2c) displayed four peaks at 530.9, 531.7, 533.2 and 535 eV, which were attributed to O-H and C=O, C-O groups and surface adsorbed  $\text{H}_2\text{O}/\text{O}_2$ , respectively [51].

For Tp-Taz, the high-resolution C 1s spectrum, four peaks can be fitted into at 284.7, 285.9, 286.6, and 288.8 eV, which assigned to C=C, C-N, C=N bonds of triazine rings, and C=O bonds of ketone, respectively. In N 1s spectrum, two peaks at 398.6 and 400.1 eV were separately assigned to nitrogen atoms in triazine groups and C-N bonds [52]. The O1s spectrum showed three peaks at 530.8, 531.9, 532.8 and 533.6 eV, which were attributed to O-H, C=O, C-O and surface adsorbed  $\text{H}_2\text{O}/\text{O}_2$ , respectively [53,54]. With regard to Tp-Tapb, the high-resolution C 1s spectrum exhibited four peaks at 284.36, 284.86, 285.93, and 287.8 eV, attributing to the C-C, C=C, C-N, C=O groups, respectively [45]. In N 1s spectrum, three peaks at 399.57, 399.96 and 400.52 eV were corresponded to N-C, N-H and C-N-C, respectively. The O1s spectrum showed three peaks at 530.7, 531.76 and 533.3 eV, which were attributed to O-H, C=O and C-O groups, respectively [55]. In terms of the above characterization results, three COFs materials were



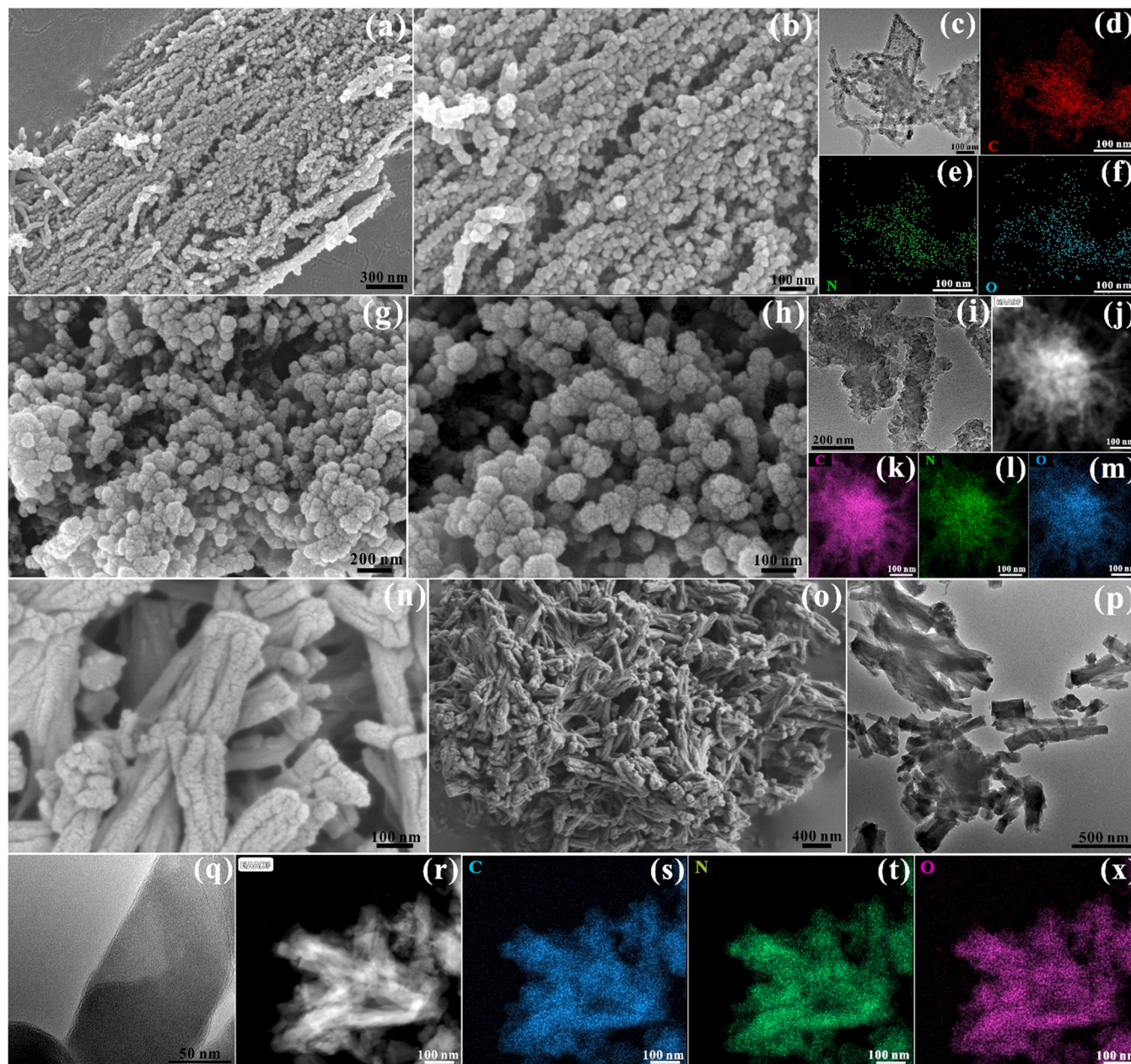


Fig. 2. SEM and TEM-mapping images of (a-f) Tp-Taz; (g-m) Tp-Tapb; (n-x) TpTt.

successfully synthesized.

As displayed in Fig. 2, Tp-Taz was the uniform wire-like morphology consisting of tiny particles, these nanowires were cross connected and stacked to form a loose porous morphology. Tp-Tapb had the spheroid morphology and was characterized by the particle size of 50–100 nm. TpTt was interwoven thread-shaped morphology with an average width of 200–500 nm.

The resultant three COFs materials showed the type IV isotherm with H4 type hysteresis loop (Fig. 3a), indicating the ordered porous structure. The Brunauer-Emmett-Teller (BET) specific surface areas of Tp-Taz, Tp-Tapb and TpTt were measured to be 861.77, 845.49 and 103.26 m<sup>2</sup>/g, respectively. Apparently, Tp-Taz and Tp-Tapb had relatively high specific surface area, which could provide more active centers and play an active role in photocatalytic reduction of U(VI). According to the TGA curves (Fig. 3b), the thermal stability of the three COFs materials were up to ~500 °C. Among them, the thermal stability of TpTt was the best, followed by Tp-Tapb, and Tp-Taz the worst. The

first-stage weight loss (30–300 °C) of COFs materials was attributed to the evaporation of a small amount of water and solvent molecules or the loss of surface functional groups, and the second-stage weight loss ( $\geq 300$  °C) was due to the decomposition of the bulk materials [56]. The three COFs materials had good temperature stability, which was very beneficial to the treatment of highly radioactive uranium containing wastewater.

### 3.2. Optical and electronic properties

The optical properties of the three COFs materials were investigated by UV-vis DRS. As shown in Fig. 4a, they all had visible-light response, and the absorption edges of Tp-Taz, Tp-Tapb and TpTt were 570, 550 and 534 nm, respectively, as well as the corresponding band gaps ( $E_g$ ) of 2.34, 2.4 and 2.58 eV (Fig. 4b-d) [57]. The absorption range of Tp-Taz was narrower than that of TpTt, due to increasing the number of peripheral benzene rings improved the conjugation extent of skeleton. The



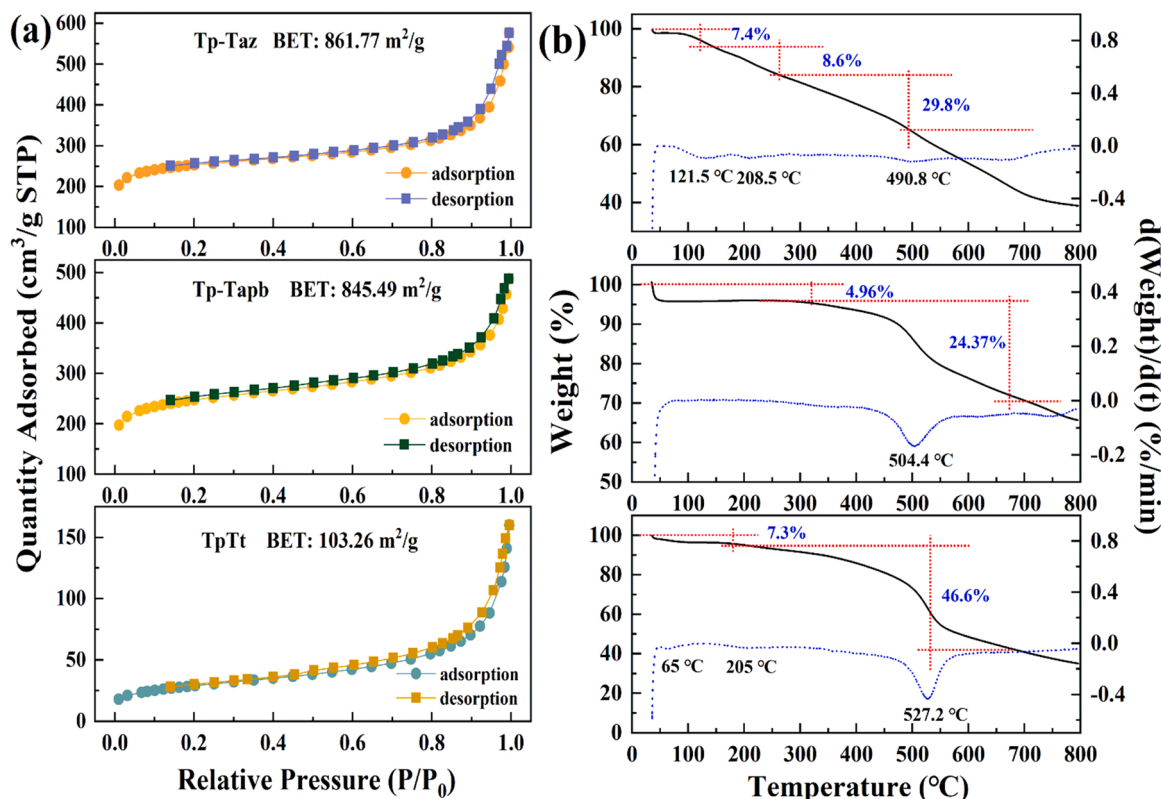


Fig. 3. The N<sub>2</sub> adsorption-desorption isotherms and TGA curves of Tp-Taz, Tp-Tapb and TpTt.

resultant three COFs materials exhibited similar optical absorption properties, but the framework structures were different due to different constructed ligands, which affected the band gaps of COFs. Moreover, the flat band potential ( $E_{FB}$ ) and the property of semiconductors (n- or p-type) can be obtained via the Mott-Schottky measurement (shown in Fig. 4e-g) [58]. The positive slopes of the Mott-Schottky plots implied that Tp-Taz, Tp-Tapb and TpTt were typical n-type semiconductors [59]. In addition, the  $E_{FB}$  values of Tp-Taz, Tp-Tapb and TpTt were estimated to be about  $-0.87$ ,  $-0.96$  and  $-0.75$  V (vs. Ag/AgCl), respectively. Generally, the valence band ( $E_{VB}$ ) of n-type semiconductors were about 0.1 more negative than that of  $E_{FB}$  [60,61]. Therefore, the  $E_{VB}$  values of Tp-Taz, Tp-Tapb and TpTt were  $-0.77$ ,  $-0.86$  and  $-0.65$  V (vs. NHE), and the corresponding conduction band ( $E_{CB}$ ) values were 1.57, 1.54 and 1.93 V (vs. NHE), respectively. Apparently, the  $E_g$  values of Tp-Taz, Tp-Tapb and TpTt were narrow enough to capture visible light, and the  $E_{CB}$  values were negative enough to enable soluble U(VI) reduced into insoluble U(IV) oxides ( $UO_2^{2+}/U^{4+}$  0.327 V vs. NHE,  $UO_2^{2+}/UO_2$  0.411 V vs. NHE) by photogenerated electrons on the CB of the irradiated three COFs materials [62].

Electron spin resonance (EPR) was applied to ascertain the produced reactive oxygen species (ROS) under light irradiation. Obviously, As shown in Fig. 5, the three COFs materials exhibited high productivity of superoxide radicals ( $\bullet O_2^-$ ) and singlet oxygen ( $^1O_2$ ), the CB corresponding to the three COFs catalysts were more negative than the  $O_2/\bullet O_2^-$  potential ( $-0.33$  V vs. NHE) [63], while the VB potentials were lower than hydroxyl radical ( $\bullet OH$ )/H<sub>2</sub>O (2.68 V vs. NHE). Thus, the three COFs materials could capture dissolved  $O_2$  to generate  $\bullet O_2^-$ , but not easy to produce  $\bullet OH$ . Moreover,  $^1O_2$  was generated in the current photocatalytic system, implying that three COFs materials were highly electron-enriched [64]. By comparing the intensity of generating  $^1O_2$ , the order of electron-enriched ability was TpTt > Tp-Taz > Tp-Tapb.

Unfortunately, the Coulomb interaction between electron ( $e^-$ )-hole ( $h^+$ ) pairs was called excitonic effect, which suppressed the charge transfer process and abated the photocatalytic efficiency. Hence it

should be considered in some optical excitation processes. The different excitonic behavior resulted in the different ROS generation. In general, the electron transfer though exciton dissociation was usually the cause of  $\bullet O_2^-$  and  $\bullet OH$  generation, while the energy transfer process was the reason for the production of  $^1O_2$  [65]. The excitonic behavior of Tp-Taz, Tp-Tapb and TpTt activated  $O_2$  to  $^1O_2$  and  $\bullet O_2^-$ , respectively, under visible-light irradiation, resulting in significantly different activity and selectivity in photocatalytic U(VI) reduction. Beyond that, as for the formation mechanism of  $^1O_2$ , it could  $\bullet O_2^-$  was oxidated by the trapped  $h^+$ , reaction (1, 2) [66]. When  $^1O_2$  is generated from  $\bullet O_2^-$  by oxidation with  $h^+$ , the produced  $^1O_2$  located on the surface of the photocatalyst, which possesses a mild redox potential ( $E^0 = 2.2$  V vs. NHE).



Furthermore, oxygen vacancies (OVs), which were the most common anion vacancy defects existed in the semiconductor materials, and could directly activate  $O_2$  to  $\bullet O_2^-$  and  $^1O_2$  [67]. As displayed in Fig. 5f, asymmetric EPR signals at  $g = 2.007$  were clearly observed in the three COFs materials, stemming from the unpaired  $\pi$ -electrons trapped on surface OVs. Meanwhile, the OVs content was consistent with the above order of electron-enriched ability (TpTt > Tp-Taz > Tp-Tapb), indicating the more effective separation of  $e^-$ - $h^+$  in the framework of TpTt.

Electrochemical impedance spectroscopy (EIS) was used to explain the separation efficiency of photoinduced  $e^-$  and  $h^+$  carriers. As depicted in Fig. 6a, the Nyquist arc radius of Tp-Taz was slightly smaller than that of TpTt and Tp-Tapb, referring to the photogenerated carriers transfer velocity in the interface of Tp-Taz were the fastest. As exhibited in Fig. 6b, the transient photocurrent of Tp-Taz was stronger than that of TpTt and Tp-Tapb, indicating that electron accumulation in Tp-Taz was higher, due to the presence of the triazine and ketone groups accelerated the charge-carrier transfer and  $e^-$ - $h^+$  separation. Afterwards, Fig. 6c revealed the photoluminescence (PL) intensity of Tp-Taz and TpTt

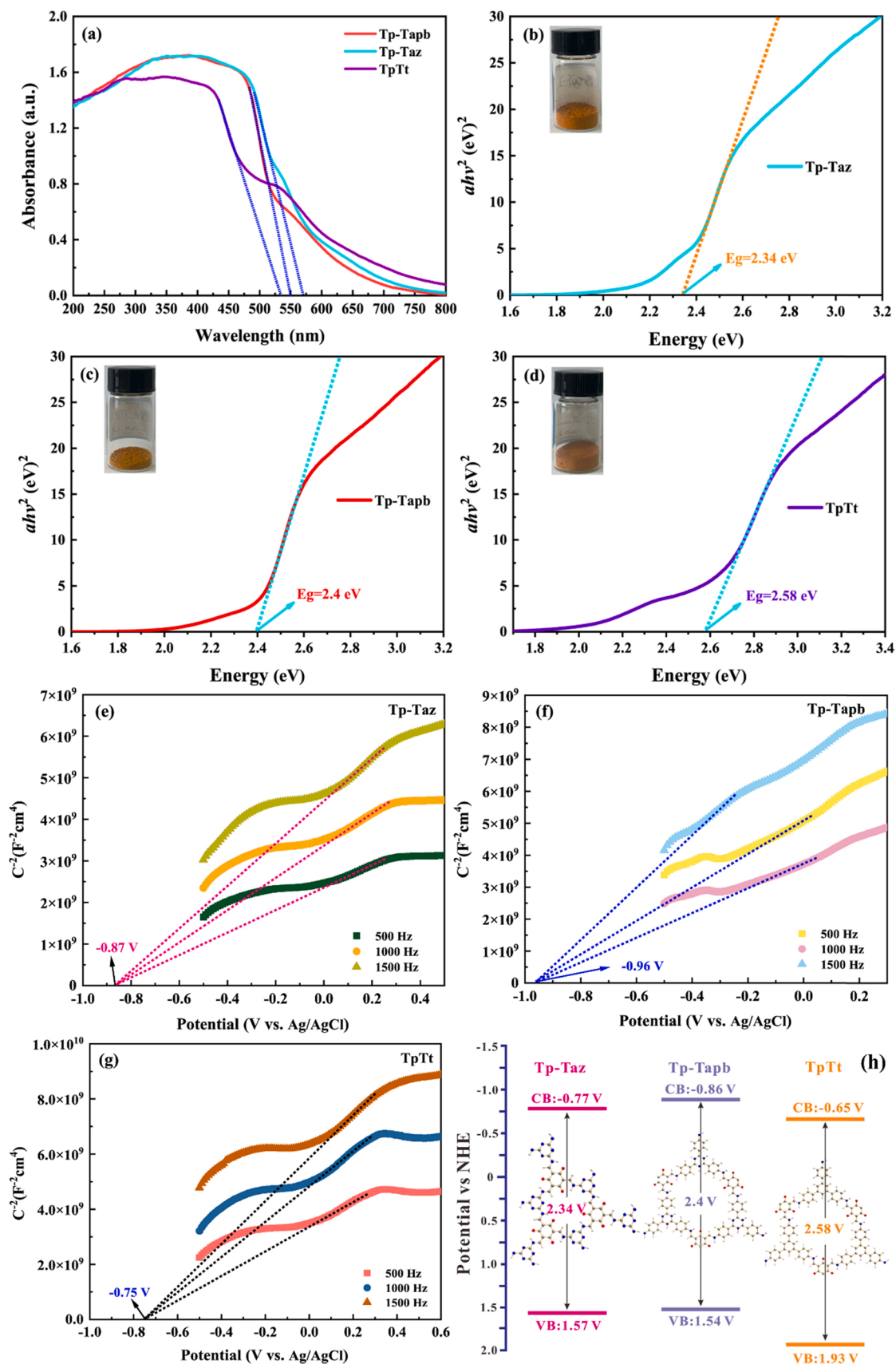


Fig. 4. (a) UV-vis absorption spectra of Tp-Taz, Tp-Tapb and TpTt; Tauc plots of (b) Tp-Taz, (c) Tp-Tapb and (d) TpTt; Mott-Schottky plots of (e) Tp-Taz, (f) Tp-Tapb and (g) TpTt; (h) the electronic band structure of Tp-Taz, Tp-Tapb and TpTt.

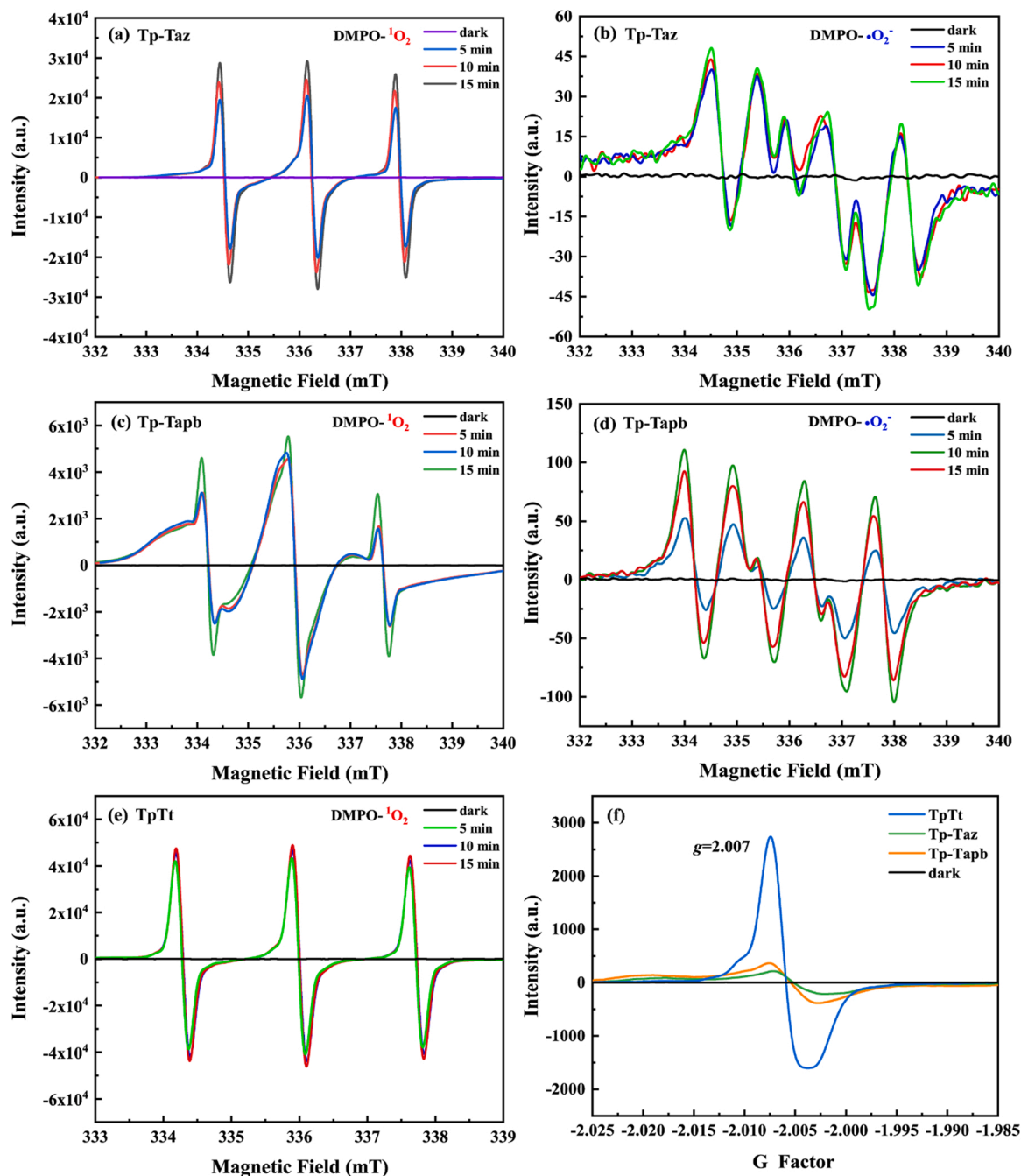


Fig. 5. EPR spectra of (a) Tp-Taz, (c) Tp-Tapb and (e) TpTt with TEMP for  $^1\text{O}_2$  trapping under different irradiation times; (b) Tp-Taz and (d) Tp-Tapb with DMPO for  $\bullet\text{O}_2$  trapping under different irradiation times; (f) EPR spectra of Tp-Taz, Tp-Tapb and TpTt.

drastically reduced, owing to the intramolecular charge transfer (ICT) by two acceptors, indicating that the photogenerated carriers were effectively separated and more photoinduced  $e^-$  participated in photocatalytic reaction.

### 3.3. Dynamic adsorption performance

Because the combination between U(VI) and photocatalyst was an important factor affecting the photoreduction performance of U(VI), the adsorption performance should be studied firstly. As shown in Fig. 7a, the primary U(VI) species were  $\text{UO}_2^{2+}$  at pH of 2.0–4.0, and the three COFs materials exhibited low adsorption performance for U(VI) due to electrostatic repulsion, because they all had O, N-containing functional groups and were easy to be protonated in the presence of a large amount

of  $\text{H}^+$ . At pH 5.0–6.5,  $\text{UO}_2^{2+}$  was hydrolyzed to  $\text{UO}_2\text{OH}^+$ ,  $(\text{UO}_2)_2(\text{OH})_2^{2+}$  and  $(\text{UO}_2)_3(\text{OH})_5^{5+}$  [62], and the adsorption capacity of Tp-Taz and TpTt for U(VI) significantly increased, then decreased at pH 7.0–8.0. Accordingly, the pH-zeta potentials relationship of three COFs materials (Fig. 7b), TpTt and Tp-Taz shown the isoelectric points around pH 4.08 and 6.07, respectively, indicating that the surfaces were negatively charged and electrostatic attraction with U(VI) hydroxylated cations. In comparison with TpTt and Tp-Taz, the  $\text{pH}_{\text{zeta}}$  value of Tp-Tapb was 7.25 and exhibited lower adsorption capacity.

The variation of adsorption capacity was associated with surface electronegativity and the distribution of U(VI) species, so the subsequent experiments were carried out at pH 6.5.

The contact time played an essential role in the adsorption process. As shown in Fig. 7c, the U(VI) adsorption capacity of the three COFs



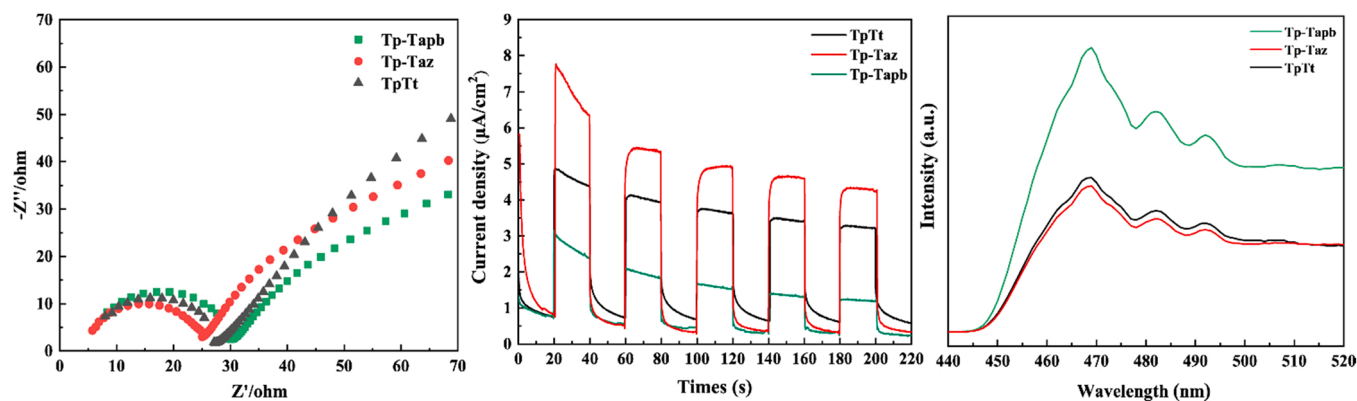


Fig. 6. (a) EIS spectra for Tp-Taz, Tp-Tapb and TpTt; (b) Steady-state PL spectra for Tp-Taz, Tp-Tapb and TpTt; (c) Transient photocurrent densities for Tp-Taz, Tp-Tapb and TpTt.

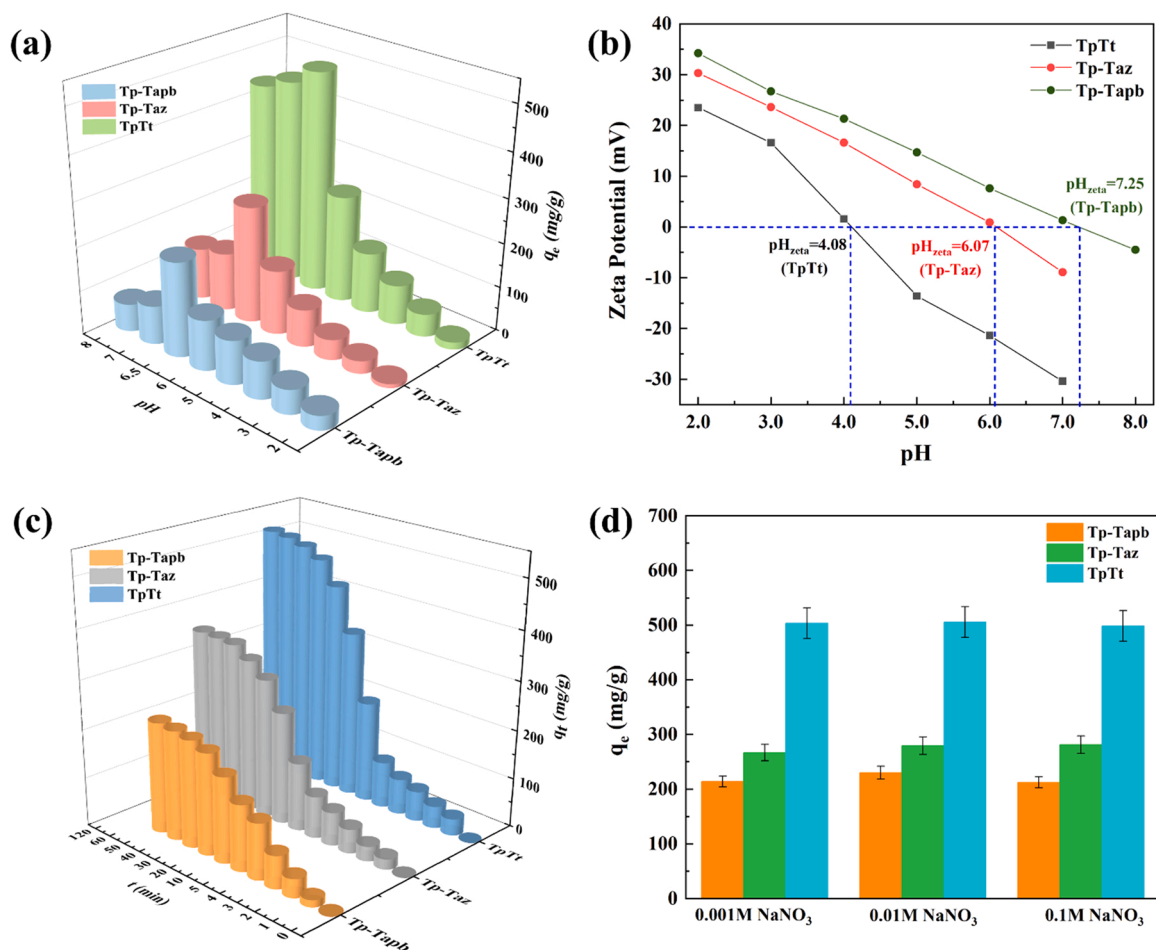


Fig. 7. (a) the influence of pH on the adsorption process, (b) Zeta Potential plots of Tp-Tapb, Tp-Taz and TpTt, (c) the effect of contact time and (d) the influence of ionic strength on the adsorption process.

materials increased sharply in the first 10 min, and achieved the adsorption equilibrium within 40 min. The order of adsorption capacity was TpTt (505 mg/g) > Tp-Taz (338 mg/g) > Tp-Tapb (227 mg/g), attributing to the high N atom contents in TpTt, which was twice that of Tp-Taz and four times that of Tp-Tapb (Table S1). As shown in Fig. S3 and Table 1, the adsorption behavior of U(VI) was further described by the pseudo-first-order and pseudo-second-order models (Eqs. (S1) and (S2), recorded in Electronic Supplementary Materials). It can be found the correlation coefficients ( $R^2$ ) of pseudo-second-order model were

higher than pseudo-first-order model, indicating that U(VI) were the chemical adsorption processes for the three COFs materials. Besides, the adsorption capacity was also affected by the initial concentration and reaction temperature, and the experimental data were simulated by Langmuir model (Eq. (S3)) and Freundlich isotherm model (Eq. (S4)). Obviously, Langmuir model was more suitable than Freundlich model (shown in Fig. S4), suggesting that the immobilization of U(VI) on the three COFs materials was monolayer adsorption and the adsorption process was heterogeneous [68]. Table 1 listed the relevant adsorption

**Table 1**

The fitting parameters of kinetic and isotherm models for U(VI) adsorption onto Tp-Tabp, Tp-Taz and TpTt.

Kinetic model parameters:							
Adsorbents	Pseudo-first-order			$R^2$	Pseudo-second-order		
	$k_1$ (min <sup>-1</sup> )	$q_e$ (mg/g)			$k_2$ (g/mg·min)	$q_e$ (mg/g)	$R^2$
Tp-Tabp	0.1186	205.41		0.9912	$9.6 \times 10^{-4}$	247.52	0.9996
Tp-Taz	0.0644	350.72		0.9961	$8.49 \times 10^{-6}$	497.51	0.9962
TpTt	0.0708	561.16		0.9921	$1.946 \times 10^{-3}$	684.93	0.9921
Adsorbents	T(K)	Langmuir model			Freundlich model		
		$q_{max}$ (mg/g)	$K_L$ (L/mg)	$R^2$	$K_F$ (mg <sup>1-1/n</sup> ·g <sup>-1</sup> ·L <sup>-1/n</sup> )	1/n	$R^2$
Tp-Tabp	298	454.78	0.0176	0.9905	21.24	0.574	0.9563
	308	473.36	0.0237	0.9983	33.20	0.507	0.9676
	318	480.34	0.0337	0.9998	51.84	0.435	0.9655
Tp-Taz	298	610.67	0.0195	0.9729	31.85	0.559	0.9170
	308	717.58	0.0243	0.9861	50.72	0.509	0.9324
	318	743.65	0.0311	0.9935	72.05	0.454	0.9385
TpTt	298	954.98	0.0137	0.9831	44.84	0.600	0.9920
	308	1201.11	0.0171	0.9882	61.42	0.5534	0.9896
	318	1220.70	0.0206	0.9941	81.06	0.5115	0.9869
Thermodynamic parameters:							
Adsorbents	T(K)	$\Delta G^0$ (kJ/mol)		$\Delta S^0$ (J/(mol·K))		$\Delta H^0$ (kJ/mol)	
Tp-Tabp	298	-8.45		114.68		25.73	
	308	-9.59					
	318	-10.74					
Tp-Taz	298	-8.63		90.96		18.48	
	308	-9.54					
	318	-10.45					
TpTt	298	-9.61		86.35		16.12	
	308	-10.48					
	318	-11.33					

**Table 2**

Comparison of various catalysts for photoreduction of U(VI).

Photocatalysts	Concentration	m/V (g/L)	Electron sacrifice	pH	Removal rate	Ref.
PTrSO-2	50 mg/L	0.5	methanol	4.0	99.5% (120 min)	[40]
BCN-80	1 mM	5	isopropanol	4.0	97.4% (90 min)	[69]
MnO <sub>2</sub> /UiO-66/Ti <sub>3</sub> C <sub>2</sub> T <sub>x</sub>	8 mg/L	0.5	none	5.0	98.4% (60 min)	[70]
MCN <sub>1.0</sub>	0.1 mM	2.0	methanol	6.0	100% (40 min)	[71]
PMo <sub>12</sub> /UiO-66	50 mg/L	0.2	methanol	5.5	98.92% (300 min)	[72]
TiO <sub>2</sub> /NHCS	10 mg/L	0.4	ethanol	5.0	90% (20 min)	[73]
Tp-Tabp	30 mg/L	0.229	methanol	5.0	25% (480 min)	This work
Tp-Taz	30 mg/L	0.229	methanol	5.0	50% (480 min)	This work
TpTt	30 mg/L	0.229	methanol	5.0	55% (480 min)	This work

thermodynamic data of three COFs materials. As the temperature rose from 25 to 45 °C, the adsorption capacities of the three COFs materials for U(VI) increased, illustrating that the adsorption procedure of U(VI) was endothermic. Meanwhile, the Gibbs free energies ( $\Delta G^0$ ) were negative (Eqs. (S5)–(S7)), indicating that the adsorption procedure of U(VI) was spontaneous. Thus, it was deemed that the adsorption procedure of the three COFs materials to U(VI) was mainly spontaneously uniform monolayer chemisorption. Table 2 displayed excellent U(VI) uptake ability compared with other U(VI) sorbents.

### 3.4. Photoreduction performance

Before turning on the light source, the three COFs materials were left for 1 h to reach absorption-desorption equilibrium of U(VI) solution. As shown in Fig. 8a, according to the results of adsorption experiments, Tp-Tabp, Tp-Taz and TpTt were left under the dark condition for 1 h, and the adsorption removal ratios were 10%, 25% and 35%, respectively. The enrichment of U(VI) was beneficial to photocatalytic reduction to achieve the synergy of adsorption and photoreduction. Clearly, the photocatalytic activities of these three COFs materials varied markedly, and the photocatalytic removal ratios of U(VI) were 25% (Tp-Tabp), 50% (Tp-Taz) and 55% (TpTt) after 10 h irradiation. Besides, the corresponding apparent reaction rate values of Tp-Tabp, Tp-Taz and TpTt were 0.036, 0.11 and 0.22 h<sup>-1</sup> based on the pseudo-first-order kinetic

equation ( $\ln(C/C_0) = kt$ ) [69], shown in Fig. S5. The photocatalytic performance of Tp-Taz and TpTt was significantly better than that of Tp-Tabp, on account of the coexistence of triazine and ketone groups increased the separation efficiency of  $e^-$ – $h^+$ . Besides, the photocatalytic activity of TpTt was twice that of Tp-Taz, demonstrating that with the increase of nitrogen atom content and the shortening of the distance between the two acceptors, the photocatalytic performance improved. The apparent quantum yield (AQY, Eqs. (S8) and (S9)) values of Tp-Tabp, Tp-Taz and TpTt were  $2.41 \times 10^{-3}\%$ ,  $7.36 \times 10^{-3}\%$  and  $1.47 \times 10^{-2}\%$ , respectively, thus improving utilization of photo-generated electrons. Compared with previously reported catalysts toward U(VI) photoreduction, the single COF material also showed relatively good catalytic activity (Table 2).

To explicate the reaction way of photocatalytic U(VI) reduction by these the three COFs materials under visible light, the radical trapping experiments were implemented under different conditions. As demonstrated in Fig. 8b–d, compared with no scavenger, the addition of methanol as  $h^+$  capture agent could improve the photocatalytic removal rate of U(VI). The effect of the addition of tert-butanol (TBA) on U(VI) photoreduction was negligible, suggesting that  $\bullet OH$  was not produced in the three COFs materials system, and there was no signal of DMPO- $\bullet OH$  adduct which was confirmed by EPR studies (Fig. 5). When the addition of *p*-benzoquinone (*p*-BQ,  $\bullet O_2$  scavenger) and KIO<sub>3</sub> (photoinduced  $e^-$  scavenger) severely inhibited photocatalytic conversion of U(VI), which

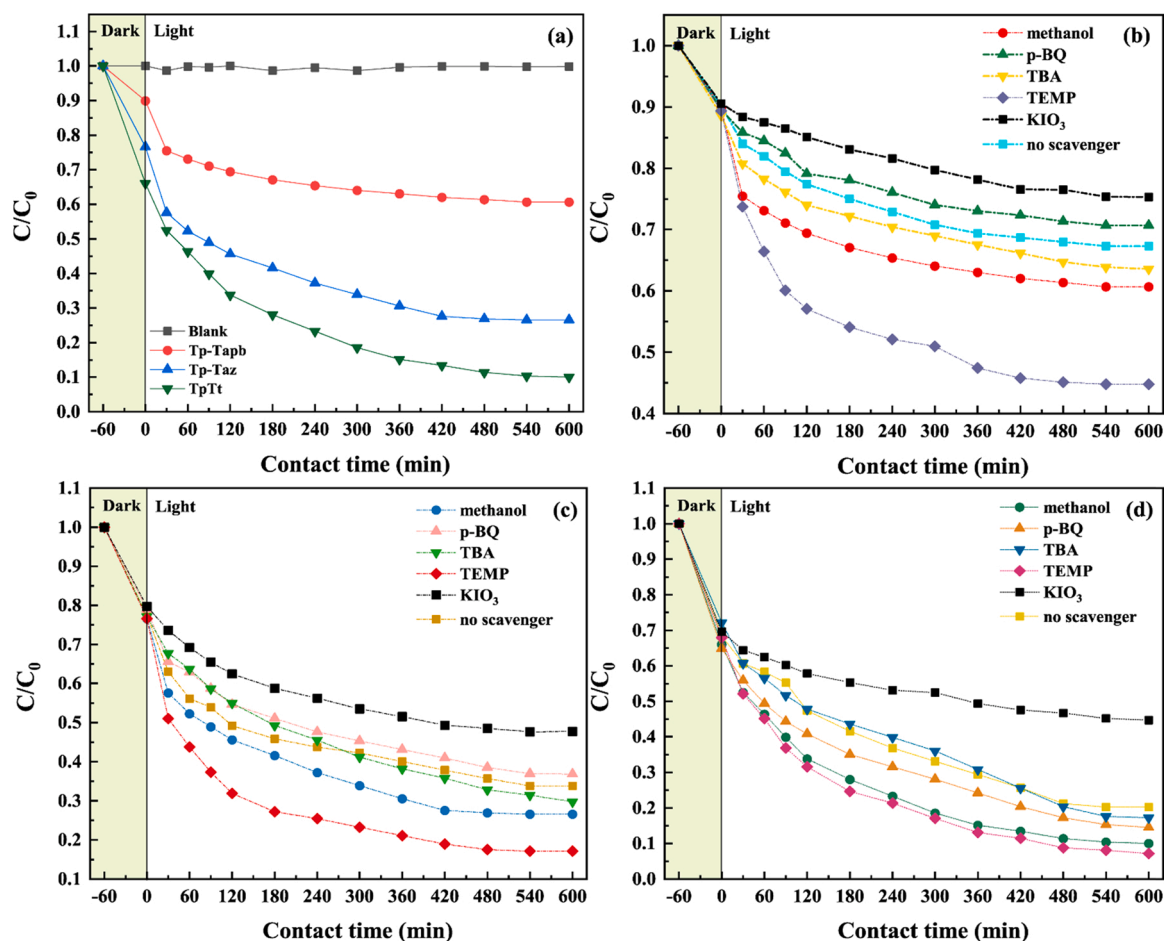


Fig. 8. (a) The photocatalytic U(VI) removal efficiencies by Tp-Tabb, Tp-Taz and TpTt ( $C_0 = 30$  mg/L,  $T = 298$  K,  $\text{pH} = 5.0$ ,  $m/V = 0.229$  g/L, adding methanol); the photocatalytic experiments with adding different sacrificial agents of (b) Tp-Tabb; (c) Tp-Taz; (d) TpTt.

demonstrated  $\bullet\text{O}_2$  and photoinduced  $e^-$  were the main reducing species for U(VI) reduction. Remarkably, in view of the oxidation and electrophilic properties of  $^1\text{O}_2$ , the addition of  $^1\text{O}_2$  scavenger 2,2,6,6-tetramethylpiperidine (TEMP) significantly improved the photocatalytic reduction of U(VI) and prevented the reoxidation of U(IV) to U(VI). Combined with Figs. 5 and 8b-d, unlike Tp-Tabb and Tp-Taz system, the presence of  $\bullet\text{O}_2$  was not detected in TpTt system, while  $^1\text{O}_2$  was observed due to reaction (1, 2). Hence, the addition of *p*-BQ in TpTt system did not strongly inhibit the photocatalytic removal rate, but the addition of TEMP greatly promoted the photocatalytic reduction reaction. However, in Tp-Tabb and Tp-Taz systems,  $\bullet\text{O}_2$  radical existed, so, the addition of *p*-BQ significantly inhibited the photocatalytic removal of U(VI). Consequently, it was again demonstrated that the main reducing species were photoinduced  $e^-$  and  $\bullet\text{O}_2$ , and the reoxidation of U(IV) into U(VI) by  $h^+$  or  $^1\text{O}_2$  should be inhibited as much as possible.

### 3.5. Removal mechanism

Comparing the XPS spectra of these the three COFs materials before and after adsorption and photoreduction, the peaks of U 4f were clearly observed, indicating that U(VI) was adsorbed to the surface of COFs materials (Fig. S6). Before photoreduction, Fig. 9a exhibited U 4f<sub>5/2</sub> (393 eV) and U 4f<sub>7/2</sub> (382.5 eV) peaks. After photoreduction, the U 4f<sub>5/2</sub> and U 4f<sub>7/2</sub> peaks could be separately subdivided into two components centered at U 4f<sub>5/2</sub> (393.7 eV 392.8 eV) and U 4f<sub>7/2</sub> (383 eV, 381.9 eV), implying the coexistence of U(IV) and U(VI) [74]. This result indirectly indicated the generated U(IV) was re-oxidized by photoinduced  $h^+$  or  $^1\text{O}_2$ . In the N 1s spectra (Fig. 9b, e), the positions of the C-N,

C-N-C and C=N=C peaks after the adsorption and photoreduction moved towards the high binding energy, suggesting that the N atoms of triazine skeleton and  $\beta$ -keto-enamine bond were bound to U. Specially, a new peak appeared in the N 1s spectra at 400.2 eV, belonging to N-U species [75]. Likewise, whether adsorption or photoreduction process, the positions of the OH, C-O and C=O peaks shifted to higher binding energy in the O 1s spectra (Fig. 9c, f), attributing to the interaction of oxygen-containing functional groups with U. The above XPS results were further corroborated by the main adsorption configurations obtained by DFT calculation (Fig. 12(a-1)–(a-7), the calculation conditions shown in the ESI). The calculated adsorption energy ( $E_{\text{ads}}$ ) was  $-1.58 \sim -2.21$  kcal/mol, and the comparatively close bond distances between U and N, O atom were  $3.0 \sim 5.0$  Å, and the adsorption sites were mainly located in the triazine structure and the hydrogen bond formed by  $\beta$ -keto-enamine. Comparing the partial density of states (PDOS) diagrams (Fig. S7) before and after adsorption, we can clearly observe that the band gap width became narrower, and the d and f orbitals of U atoms participated in hybridization, demonstrating the electron transfer.

In addition, the excellent U(VI) adsorption and photoreduction performance on Tp-Tabb, Tp-Taz and TpTt was observed after four cycle runs (Fig. S8). The stability of three COF materials was characterized by XRD (Fig. 10) and TEM-mapping (Fig. 11), no obvious change or disappearance of characteristic peaks positions was observed after four cycle runs. Meanwhile, the existing forms of U(VI) after adsorption and photoreduction were further analyzed. As shown in Fig. 10, after adsorption, U(VI) mainly existed in the form of  $\text{UO}_3 \cdot \text{H}_2\text{O}$  (meta-schoepite, PDF#43-0364) and  $\text{Na}_2(\text{UO}_2)_6(\text{OH})_{14} \cdot 4\text{H}_2\text{O}$  (PDF#36-0117). However, after photoreduction, the typical peaks of  $\text{UO}_2$  were observed



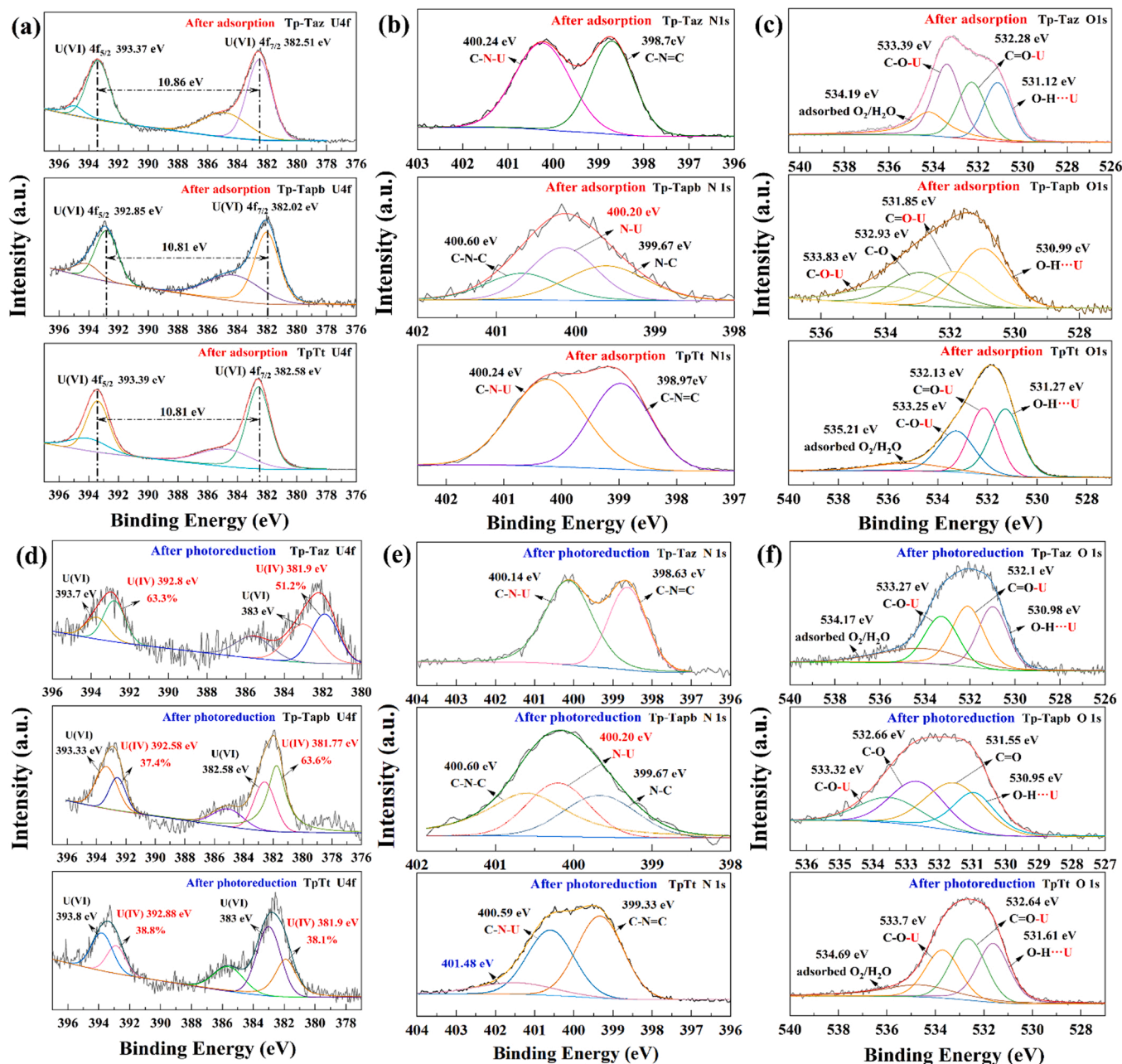


**Fig. 9.** The high-resolution XPS spectra of Tp-Taz, Tp-Tapb and TpTt: (a) U4f (b) N 1s and (c) O 1s after adsorption, and the high-resolution XPS spectra of Tp-Taz, Tp-Tapb and TpTt: (d) U4f (e) N 1s and (f) O 1s after photoreduction.

at  $\sim 10.5^\circ$ ,  $23.1^\circ$  and  $32.4^\circ$ , indicating that the conversion of U(VI) to  $\text{UO}_2(\text{s})$  (PDF#35-0834), as well as  $\text{UO}_3 \cdot \text{H}_2\text{O}$  also could be further reduced to form  $\text{UO}_2(\text{s})$  [71]. In addition, the characteristic peaks of  $\text{UO}_{2.9}$  (PDF#49-1389),  $\text{UO}_{2.87}$  (PDF#46-0950) and  $\text{UO}_{2.82}$  (PDF#09-0208) were also observed, demonstrating U(VI) was transformed into low-valent uranium precipitates during photoreduction [76, 77]. Among them, no clear peaks of uranium minerals were detected in the XRD pattern after TpTt adsorption. Meanwhile, no reduced state peaks of uranium minerals were observed in the XRD pattern after Tp-Tapb photocatalysis. This result was consistent with the above photocatalytic kinetic experiment. Compared with Tp-Tapb, Tp-Taz and TpTt shown the better photocatalytic performance and could further photocatalytic reduce the adsorbed U(VI).

Summarizing the forementioned results, the immobilization-

photoreduction mechanism of U(VI) over COFs skeleton could be deduced in Fig. 12. Firstly, U(VI) was adsorbed onto the COFs skeleton due to the existence of triazine and ketone groups. Secondly, the photoinduced  $e^-$   $h^+$  were generated by three COFs materials under illumination. However, due to the difference in the number of conjugated benzene rings, heteroatoms and acceptors, as well as the distance between acceptors, the light-response range, the band gap structure, the current intensity and the species, and intensity of ROS ( $\bullet\text{O}_2$ ,  $^1\text{O}_2$ , OV) were different. Among them, TpTt possessed the highly conjugated skeleton structure, contained the high content of N atoms, and two acceptor units with the short distance, so it shown superior adsorption and photocatalytic reduction performance for U(VI). Ultimately, the adsorbed U(VI) was simultaneously reduced efficiently to insoluble U(IV) by the photoinduced electrons and  $\bullet\text{O}_2$ , storing in COFs open space.

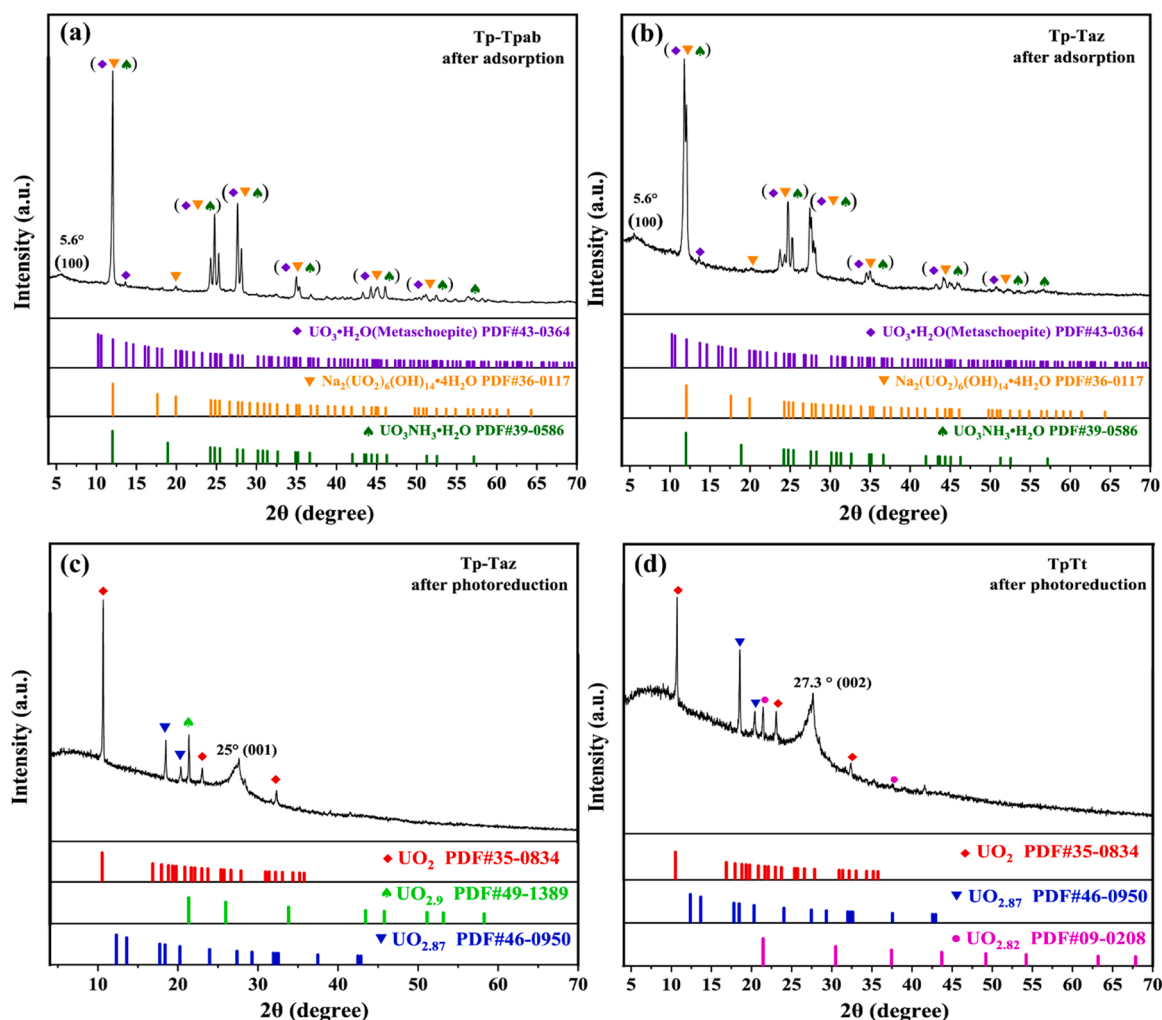


Fig. 10. The XRD patterns of (a) Tp-Tapb and (b) Tp-Taz after adsorption, and the XRD patterns of (c) Tp-Taz and (d) TpTt after photoreduction.

#### 4. Conclusion

In this work, three  $\beta$ -keto-enamine COFs comprising different electron acceptors and the distance between the two acceptors were assessed the adsorption and photoreduction performances for U(VI) removal. Among the as-synthesized COFs, TpTt possessed two short-range acceptor units (triazine and ketone) with the high content of heteroatoms, which exhibited the highest adsorption (505 mg/g) and photoreduction ( $0.22 \text{ h}^{-1}$ ) performances. These observations stemmed from the fact that the coexistence of triazine and ketone groups improved the planarity and conjugation extent of frameworks, enhanced the light absorption capacity, and boosted the efficiency of  $e^-$ - $h^+$  separation, thus improving utilization of photogenerated  $e^-$ . The photocatalytic reduction of U(VI) by these three COFs materials, U(VI) was photo-reduced by  $e^-$  and  $\bullet\text{O}_2$  in the frameworks of photoactive COFs under visible-light irradiation, so then the insoluble U(IV) species ( $\text{UO}_2$ ,  $\text{UO}_{2.9}$ ,  $\text{UO}_{2.87}$ ,  $\text{UO}_{2.82}$ ) were deposited in the open channels. The relationship between the structure and properties of the materials was comprehensive and complex. This work not only provided a new idea for U(VI) removal, but also provided a reference for the construction of COFs skeleton structure

with adjustable and efficient photocatalytic performance.

#### CRediT authorship contribution statement

**Xin Zhong:** Conceptualization, Methodology, Writing – original draft, Visualization, Funding acquisition. **Qian Ling:** Formal analysis, Validation, Investigation, Resources. **Zhenyu Ren:** Formal analysis, Validation, Investigation, Resources. **Baowei Hu:** Supervision, Project administration, Funding acquisition.

#### Declaration of Competing Interest

The authors declare that they have no known competing financial interests or personal relationships that could have appeared to influence the work reported in this paper.

#### Data availability

Data will be made available on request.



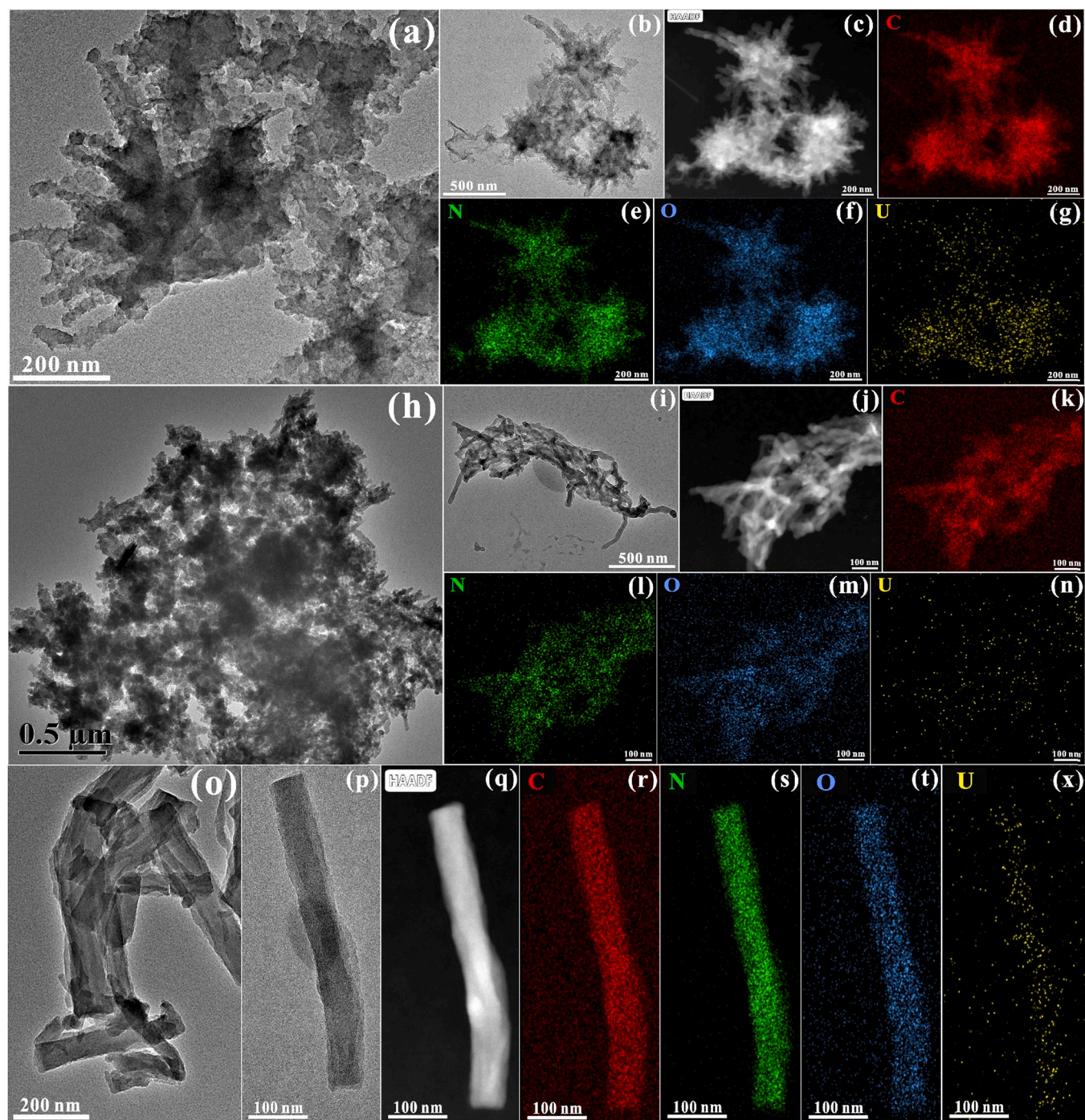
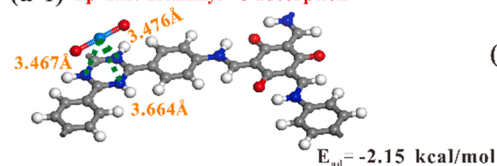


**Fig. 11.** TEM-mapping images of (a-g) Tp-Tapb; (h-n) Tp-Taz; (o-x) TpTt after U(VI) photoreduction.

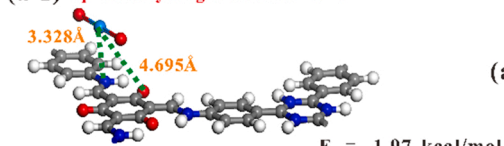


## Adsorption mechanism: $E_{ad(TpTt-U)} < E_{ad(TpTaz-U)} < E_{ad(TpTapb-U)}$

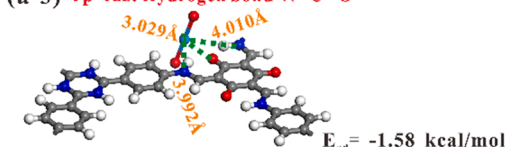
(a-1) Tp-Taz: Triazinyl--U adsorption



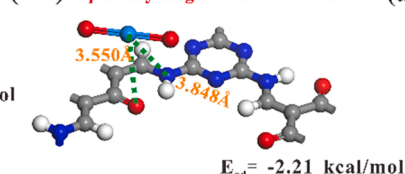
(a-2) Tp-Taz: Hydrogen bond N--U--O



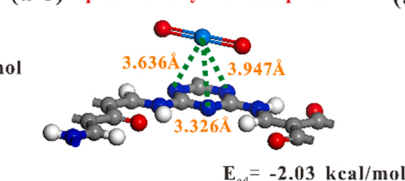
(a-3) Tp-Taz: Hydrogen bond N--U--O



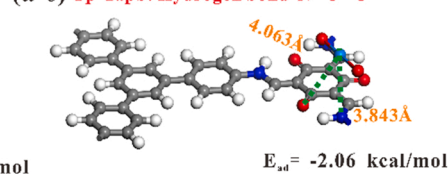
(a-4) TpTt: Hydrogen bond N--U--O



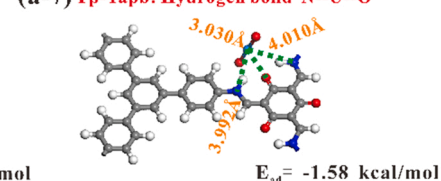
(a-5) TpTt: Triazinyl--U adsorption



(a-6) Tp-Tapb: Hydrogen bond N--U--O



(a-7) Tp-Tapb: Hydrogen bond N--U--O



## Photoreduction mechanism:

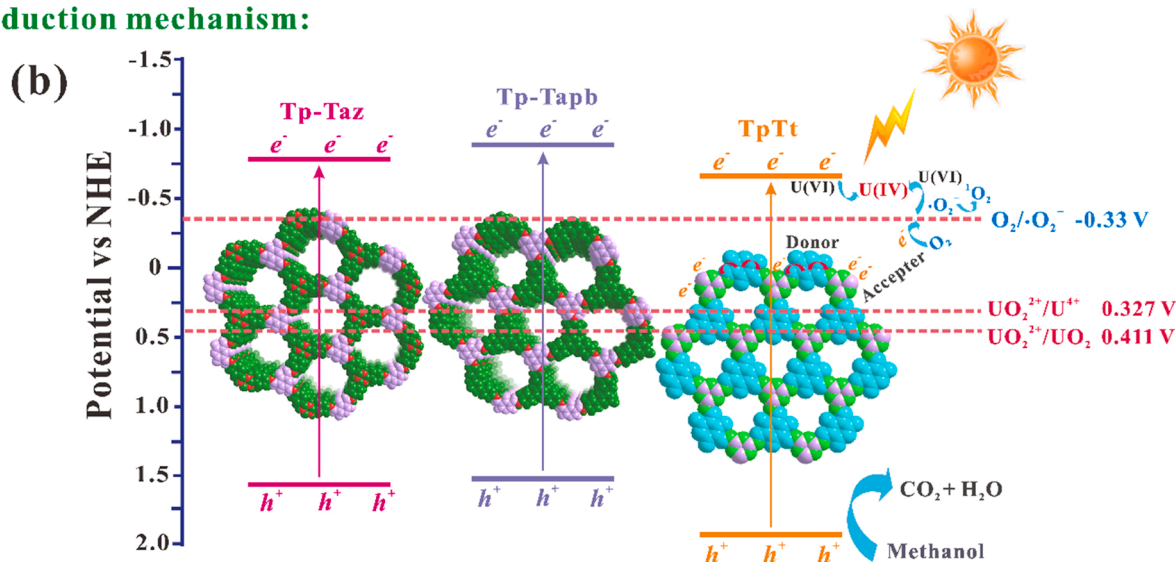


Fig. 12. The immobilization-photoreduction mechanism of U(VI) over COFs skeleton.

## Acknowledgments

We sincerely appreciate the "leading talent training plan of colleges and universities in Zhejiang Province". Financial support from the Research Fund Program of National Natural Science Foundation of China (No. 22106107).

## Appendix A. Supplementary material

Supplementary data associated with this article can be found in the online version at doi:10.1016/j.apcatb.2023.122398.

## References

- [1] L. Feng, Y. Yuan, B. Yan, T. Feng, Y. Jian, J. Zhang, W. Sun, K. Lin, G. Luo, N. Wang, Halogen hydrogen-bonded organic framework (XHOF) constructed by singlet open-shell diradical for efficient photoreduction of U(VI), *Nat. Commun.* 13 (2022) 1389.
- [2] Y. Yuan, S. Zhao, J. Wen, D. Wang, X. Guo, L. Xu, X. Wang, N. Wang, Rational design of porous nanofiber adsorbent by blow-spinning with ultrahigh uranium recovery capacity from seawater, *Adv. Funct. Mater.* 29 (2019) 1805380.
- [3] X. Zhong, Y. Liu, S. Wang, Y. Zhu, B. Hu, In-situ growth of COF on BiOBr 2D material with excellent visible-light-responsive activity for U(VI) photocatalytic reduction, *Sep. Purif. Technol.* (2021), 119627.
- [4] X. Zhong, Z. Lu, W. Liang, X. Guo, B. Hu, The fabrication of 3D hierarchical flower-like 8-MnO<sub>2</sub>@COF nanocomposites for the efficient and ultra-fast removal of UO<sub>2</sub><sup>2+</sup> ions from aqueous solution, *Environ. Sci. Nano* 7 (2020) 3303–3317.
- [5] S. Liu, Z. Wang, Y. Lu, H. Li, X. Chen, G. Wei, T. Wu, D.J. Maguire, G. Ye, J. Chen, Sunlight-induced uranium extraction with triazine-based carbon nitride as both photocatalyst and adsorbent, *Appl. Catal. B Environ.* 282 (2021), 119523.
- [6] X. Zhong, W. Liang, H. Wang, C. Xue, B. Hu, Aluminum-based metal-organic frameworks (CAU-1) highly efficient UO<sub>2</sub><sup>2+</sup> and TcO<sub>4</sub><sup>-</sup> ions immobilization from aqueous solution, *J. Hazard. Mater.* 407 (2021), 124729.
- [7] Y. Yuan, Q. Yu, S. Yang, J. Wen, Z. Guo, X. Wang, N. Wang, Ultrafast recovery of uranium from seawater by *Bacillus velezensis* strain UUS-1 with innate anti-biofouling activity, *Adv. Sci.* 6 (2019) 1900961.
- [8] D. Ma, X. Xu, Z. Li, H. Peng, D. Cai, D. Wang, Q. Yue, Nanoemulsion assembly toward vaterite mesoporous CaCO<sub>3</sub> for high-efficient uranium extraction from seawater, *J. Hazard. Mater.* 432 (2022), 128695.
- [9] X. Zhong, Y. Liu, W. Zeng, Y. Zhu, B. Hu, Excellent photoreduction performance of U(VI) on metal organic framework/covalent organic framework heterojunction by solar-driven, *Sep. Purif. Technol.* 285 (2022), 120405.
- [10] H. Li, S. Wang, Reaction: semiconducting MOFs offer new strategy for uranium extraction from seawater, *Chem* 7 (2021) 279–280.
- [11] M. Chen, T. Liu, X. Zhang, R. Zhang, S. Tang, Y. Yuan, Z. Xie, Y. Liu, H. Wang, K. V. Fedorovich, N. Wang, Photoinduced enhancement of uranium extraction from seawater by MOF/black phosphorus quantum dots heterojunction anchored on cellulose nanofiber aerogel, *Adv. Funct. Mater.* 31 (2021) 2100106.

- [12] T. Chen, B. Liu, M. Li, L. Zhou, D. Lin, X. Ding, J. Lian, J. Li, R. He, T. Duan, W. Zhu, Efficient uranium reduction of bacterial cellulose-MoS<sub>2</sub> heterojunction via the synergistically effect of Schottky junction and S-vacancies engineering, *Chem. Eng. J.* 406 (2021), 126791.
- [13] H. Wang, H. Guo, N. Zhang, Z. Chen, B. Hu, X. Wang, Enhanced photoreduction of U(VI) on C<sub>3</sub>N<sub>4</sub> by Cr(VI) and Bisphenol A: ESR, XPS, and EXAFS investigation, *Environ. Sci. Technol.* 53 (2019) 6454–6461.
- [14] J. Wang, Y. Wang, W. Wang, T. Peng, J. Liang, P. Li, D. Pan, Q. Fan, W. Wu, Visible light driven Ti<sup>3+</sup> self-doped TiO<sub>2</sub> for adsorption-photocatalysis of aqueous U(VI), *Environ. Pollut.* 262 (2020), 114373.
- [15] Z. Li, Z. Zhang, Z. Dong, Y. Wu, X. Zhu, Z. Cheng, Y. Liu, Y. Wang, Z. Zheng, X. Cao, Y. Wang, Y. Liu, CuS/TiO<sub>2</sub> nanotube arrays heterojunction for the photoreduction of uranium (VI), *J. Solid State Chem.* 303 (2021), 122499.
- [16] J. Lei, H. Liu, C. Yuan, Q. Chen, J.-A. Liu, F. Wen, X. Jiang, W. Deng, X. Cui, T. Duan, W. Zhu, R. He, Enhanced photoreduction of U(VI) on WO<sub>3</sub> nanosheets by oxygen defect engineering, *Chem. Eng. J.* 416 (2021), 129164.
- [17] W. Qiu, Y. He, L. Li, Z. Liu, S. Zhong, Y. Yu, Donor-acceptor pairs in covalent organic frameworks promoting electron transfer for metal-free photocatalytic organic synthesis, *Langmuir* 37 (2021) 11535–11543.
- [18] S. Wang, G. Wei, Y. Xie, H. Shang, Z. Chen, H. Wang, H. Yang, G.I.N. Waterhouse, X. Wang, Constructing nanotraps in covalent organic framework for uranium sequestration, *Sep. Purif. Technol.* 303 (2022), 122256.
- [19] X. Li, Y. Qi, G. Yue, Q. Wu, Y. Li, M. Zhang, X. Guo, X. Li, L. Ma, S. Li, Solvent- and catalyst-free synthesis of an azine-linked covalent organic framework and the induced tautomerization in the adsorption of U(VI) and Hg(II), *Green Chem.* 21 (2019) 649–657.
- [20] S. Yang, H. Lv, H. Zhong, D. Yuan, X. Wang, R. Wang, Transformation of covalent organic frameworks from N-acylhydrazones to oxadiazole linkages for smooth electron transfer in photocatalysis, *Angew. Chem. Int. Ed. Engl.* 61 (2022), e202115655.
- [21] W. Helweh, N.C. Flanders, S. Wang, B.T. Phelan, P. Kim, M.J. Strauss, R.L. Li, M. S. Kelley, M.S. Kirschner, D.O. Edwards, A.P. Spencer, G.C. Schatz, R.D. Schaller, W.R. Dichtel, L.X. Chen, Layered structures of assembled imine-linked macrocycles and two-dimensional covalent organic frameworks give rise to prolonged exciton lifetimes, *J. Mater. Chem. C* 10 (2022) 3015–3026.
- [22] S.Y. Hu, Y.N. Sun, Z.W. Feng, F.O. Wang, Y.K. Lv, Design and construction strategies to improve covalent organic frameworks photocatalyst's performance for degradation of organic pollutants, *Chemosphere* 286 (2022), 131646.
- [23] X. Ren, G. Liao, Z. Li, H. Qiao, Y. Zhang, X. Yu, B. Wang, H. Tan, L. Shi, X. Qi, H. Zhang, Two-dimensional MOF and COF nanosheets for next-generation optoelectronic applications, *Coord. Chem. Rev.* 435 (2021), 213781.
- [24] X. Zhao, P. Pachfule, A. Thomas, Covalent organic frameworks (COFs) for electrochemical applications, *Chem. Soc. Rev.* 50 (2021) 6871–6913.
- [25] W.R. Cui, C.R. Zhang, R.H. Xu, X.R. Chen, W. Jiang, Y.J. Li, R.P. Liang, L. Zhang, J. D. Qiu, Rational design of covalent organic frameworks as a groundbreaking uranium capture platform through three synergistic mechanisms, *Appl. Catal. B Environ.* 294 (2021), 120250.
- [26] Y. Zhi, Z. Li, X. Feng, H. Xia, Y. Zhang, Z. Shi, Y. Mu, X. Liu, Covalent organic frameworks as metal-free heterogeneous photocatalysts for organic transformations, *J. Mater. Chem. A* 5 (2017) 22933–22938.
- [27] M.Y. Gao, C.C. Li, H.L. Tang, X.J. Sun, H. Dong, F.-M. Zhang, Boosting visible-light-driven hydrogen evolution of covalent organic frameworks through compositing with MoS<sub>2</sub>: a promising candidate for noble-metal-free photocatalysts, *J. Mater. Chem. A* 7 (2019) 20193–20200.
- [28] J.L. Sheng, H. Dong, X.B. Meng, H.L. Tang, Y.H. Yao, D.Q. Liu, L.L. Bai, F.M. Zhang, J.Z. Wei, X.J. Sun, Effect of different functional groups on photocatalytic hydrogen evolution in covalent-organic frameworks, *ChemCatChem* 11 (2019) 2313–2319.
- [29] J. Zhang, Y. Cao, W. Liu, T. Cao, J. Qian, J. Wang, X. Yao, A. Iqbal, W. Qin, Structural engineering of covalent organic frameworks comprising two electron acceptors improves photocatalytic performance, *ChemSusChem* 15 (2022), e202101510.
- [30] L. Peng, S. Chang, Z. Liu, Y. Fu, R. Ma, X. Lu, F. Zhang, W. Zhu, L. Kong, M. Fan, Visible-light-driven photocatalytic CO<sub>2</sub> reduction over ketonamine-based covalent organic frameworks: role of the host functional groups, *Catal. Sci. Technol.* 11 (2021) 1717–1724.
- [31] H. Shan, D. Cai, X. Zhang, Q. Zhu, P. Qin, J. Baeyens, Donor-acceptor type two-dimensional porphyrin-based covalent organic framework for visible-light-driven heterogeneous photocatalysis, *Chem. Eng. J.* 432 (2022), 134288.
- [32] Y. Liu, Y. Wang, H. Li, X. Guan, L. Zhu, M. Xue, Y. Yan, V. Valtchev, S. Qiu, Q. Fang, Ambient aqueous-phase synthesis of covalent organic frameworks for degradation of organic pollutants, *Chem. Sci.* 10 (2019) 10815–10820.
- [33] G. Liu, G. Pan, Q. Dang, R. Li, L. Li, C. Yang, Y. Yu, Hollow covalent organic framework cages with Zn ion-implantation promoting photocatalytic H<sub>2</sub> evolution, *ChemCatChem* 14 (2022), e202101800.
- [34] X. Lin, Y. Deng, Y. He, J. Chen, S. Hu, Construction of hydrophilic N, O-rich carboxylated triazine-covalent organic frameworks for the application in selective simultaneous electrochemical detection, *Appl. Surf. Sci.* 545 (2021), 149047.
- [35] R. Lu, C. Liu, Y. Chen, L. Tan, G. Yuan, P. Wang, C. Wang, H. Yan, Effect of linkages on photocatalytic H<sub>2</sub> evolution over covalent organic frameworks, *J. Photochem. Photobiol. A Chem.* 421 (2021), 113546.
- [36] L. Yin, Y. Zhao, Y. Xing, H. Tan, Z. Lang, W. Ho, Y. Wang, Y. Li, Structure-property relationship in  $\beta$ -keto-enamine-based covalent organic frameworks for highly efficient photocatalytic hydrogen production, *Chem. Eng. J.* 419 (2021), 129984.
- [37] J. Yang, A. Acharjya, M.Y. Ye, J. Rabeah, S. Li, Z. Kochovski, S. Youk, J. Roesser, J. Gruneberg, C. Penschke, M. Schwarze, T. Wang, Y. Lu, R. van de Krol, M. Oschatz, R. Schomacker, P. Saalfrank, A. Thomas, Protonated imine-linked covalent organic frameworks for photocatalytic hydrogen evolution, *Angew. Chem. Int. Ed. Engl.* (2021) 2–9.
- [38] K. Lei, D. Wang, L. Ye, M. Kou, Y. Deng, Z. Ma, L. Wang, Y. Kong, A. Metal-Free, Donor-acceptor covalent organic framework photocatalyst for visible-light-driven reduction of CO<sub>2</sub> with H<sub>2</sub>O, *ChemSusChem* 13 (2020) 1725–1729.
- [39] G.A. Leith, A.M. Rice, B.J. Yarbrough, A.A. Berseneva, R.T. Ly, C.N. Buck 3rd, D. Chusov, A.J. Brandt, D.A. Chen, B.W. Lamm, M. Stefik, K.S. Stephenson, M. D. Smith, A.K. Vannucci, P.J. Pellechia, S. Garashchuk, N.B. Shustova, A dual threat: redox-activity and electronic structures of well-defined donor-acceptor fullerene covalent-organic materials, *Angew. Chem. Int. Ed. Engl.* 59 (2020) 6000–6006.
- [40] F. Yu, Z. Zhu, S. Wang, J. Wang, Z. Xu, F. Song, Z. Dong, Z. Zhang, Novel donor-acceptor-acceptor ternary conjugated microporous polymers with boosting forward charge separation and suppressing backward charge recombination for photocatalytic reduction of uranium (VI), *Appl. Catal. B Environ.* 301 (2022), 120819.
- [41] R. Gomes, A. Bhaumik, A new triazine functionalized luminescent covalent organic framework for nitroaromatic sensing and CO<sub>2</sub> storage, *RSC Adv.* 6 (2016) 28047–28054.
- [42] M. Bhadra, S. Kandambeth, M.K. Sahoo, M. Addicoat, E. Balaraman, R. Banerjee, Triazine functionalized porous covalent organic framework for photo-organocatalytic E-Z isomerization of olefins, *J. Am. Chem. Soc.* 141 (2019) 6152–6156.
- [43] D. Kaleeswaran, P. Vishnoi, R. Murugavel, [3+3] Imine and  $\beta$ -ketonamine tethered fluorescent covalent-organic frameworks for CO<sub>2</sub> uptake and nitroaromatic sensing, *J. Mater. Chem. C* 3 (2015) 7159–7171.
- [44] D. Lin, P. Duan, W. Yang, X. Huang, Y. Zhao, C. Wang, Q. Pan, Facile fabrication of melamine sponge@covalent organic framework composite for enhanced degradation of tetracycline under visible light, *Chem. Eng. J.* 430 (2022), 132817.
- [45] L. Yang, Y. Song, C. Lin, L. Hou, L. Guo, Y. Lei, L. Wang, Fluorescent core-shell SiO<sub>2</sub>@vertical covalent organic framework nanosheets for sensing application, *Sens. Actuators B Chem.* 341 (2021), 129995.
- [46] H. Lv, X. Zhao, H. Niu, S. He, Z. Tang, F. Wu, J.P. Giesy, Ball milling synthesis of covalent organic framework as a highly active photocatalyst for degradation of organic contaminants, *J. Hazard. Mater.* 369 (2019) 494–502.
- [47] J. Wang, Y. Yu, J. Cui, X. Li, Y. Zhang, C. Wang, X. Yu, J. Ye, Defective g-C<sub>3</sub>N<sub>4</sub>/covalent organic framework van der Waals heterojunction toward highly efficient S-scheme CO<sub>2</sub> photoreduction, *Appl. Catal. B Environ.* 301 (2022), 120814.
- [48] J. Wang, X.X. Tian, L. Yu, D.J. Young, W.B. Wang, H.Y. Li, H.X. Li, Engineering structural defects into a covalent organic framework for enhanced photocatalytic activity, *J. Mater. Chem. A* 9 (2021) 25474–25479.
- [49] C. Li, H. Li, C. Li, X. Ren, Q. Yang, One-pot synthesis of mesosilica/nano covalent organic polymer composites and their synergistic effect in photocatalysis, *Chin. J. Catal.* 42 (2021) 1821–1830.
- [50] S. He, Q. Rong, H. Niu, Y. Cai, Construction of a superior visible-light-driven photocatalyst based on a C<sub>3</sub>N<sub>4</sub> active centre-photoelectron shift platform-electron withdrawing unit triadic structure covalent organic framework, *Chem. Commun.* 53 (2017) 9636–9639.
- [51] M.Y. Zhang, J.K. Li, R. Wang, S.N. Zhao, S.Q. Zang, T.C.W. Mak, Construction of core-shell MOF@COF hybrids with controllable morphology adjustment of COF shell as a novel platform for photocatalytic cascade reactions, *Adv. Sci.* 8 (2021), e2101884.
- [52] Y. Wang, Q. Yang, F. Yi, R. Lu, Y. Chen, C. Liu, X. Li, C. Wang, H. Yan, NH<sub>2</sub>-UiO-66 coated with two-dimensional covalent organic frameworks: high stability and photocatalytic activity, *ACS Appl. Mater. Interfaces* 13 (2021) 29916–29925.
- [53] M.C. Daugherty, E. Vitaku, R.L. Li, A.M. Evans, A.D. Chavez, W.R. Dichtel, Improved synthesis of beta-ketonamine-linked covalent organic frameworks via monomer exchange reactions, *Chem. Commun.* 55 (2019) 2680–2683.
- [54] Z. Li, H. Fang, Z. Chen, W. Zou, C. Zhao, X. Yang, Regulating donor-acceptor interactions in triazine-based conjugated polymers for boosted photocatalytic hydrogen production, *Appl. Catal. B Environ.* 312 (2022), 121374.
- [55] J. Cao, W. Shan, Q. Wang, X. Ling, G. Li, Y. Lyu, Y. Zhou, J. Wang, Ordered porous poly(ionic liquid) crystallites: spacing confined ionic surface enhancing selective CO<sub>2</sub> capture and fixation, *ACS Appl. Mater. Interfaces* 11 (2019) 6031–6041.
- [56] Y.H. Yao, J. Li, H. Zhang, H.L. Tang, L. Fang, G.D. Niu, X.J. Sun, F.M. Zhang, Facile synthesis of a covalently connected rGO-COF hybrid material by in situ reaction for enhanced visible-light induced photocatalytic H<sub>2</sub> evolution, *J. Mater. Chem. A* 8 (2020) 8949–8956.
- [57] H. Zhang, W. Liu, A. Li, D. Zhang, X. Li, F. Zhai, L. Chen, L. Chen, Y. Wang, S. Wang, Three mechanisms in one material: uranium capture by a polyoxometalate-organic framework through combined complexation, chemical reduction, and photocatalytic reduction, *Angew. Chem. Int. Ed. Engl.* 58 (2019) 16110–16114.
- [58] L. Sun, L. Li, J. Fan, Q. Xu, D. Ma, Construction of highly active WO<sub>3</sub>/TpPa-1-COF S-scheme heterojunction toward photocatalytic H<sub>2</sub> generation, *J. Mater. Sci. Technol.* 123 (2022) 41–48.
- [59] C. Liu, S. Mao, H. Wang, Y. Wu, F. Wang, M. Xia, Q. Chen, Peroxymonosulfate-assisted for facilitating photocatalytic degradation performance of 2D/2D WO<sub>3</sub>/BiOBr S-scheme heterojunction, *Chem. Eng. J.* 430 (2022), 132806.
- [60] H.Y. Zhang, Y. Yang, C.C. Li, H.L. Tang, F.M. Zhang, G.L. Zhang, H. Yan, A new strategy for constructing covalently connected MOF@COF core-shell heterostructures for enhanced photocatalytic hydrogen evolution, *J. Mater. Chem. A* 9 (2021) 16743–16750.
- [61] S. Li, M. Cai, C. Wang, Y. Liu, N. Li, P. Zhang, X. Li, Rationally designed Ta<sub>3</sub>N<sub>5</sub>/BiOCl S-scheme heterojunction with oxygen vacancies for elimination of

- tetracycline antibiotic and Cr(VI): performance, toxicity evaluation and mechanism insight, *J. Mater. Sci. Technol.* 123 (2022) 177–190.
- [62] Z. Dong, Z. Zhang, Z. Li, Y. Feng, W. Dong, T. Wang, Z. Cheng, Y. Wang, Y. Dai, X. Cao, Y. Liu, Y. Liu, 3D structure aerogels constructed by reduced graphene oxide and hollow TiO<sub>2</sub> spheres for efficient visible-light-driven photoreduction of U(VI) in air-equilibrated wastewater, *Environ. Sci. Nano* 8 (2021) 2372–2385.
- [63] Y. Yang, Z. Bian, Oxygen doping through oxidation causes the main active substance in g-C<sub>3</sub>N<sub>4</sub> photocatalysis to change from holes to singlet oxygen, *Sci. Total Environ.* 753 (2021), 141908.
- [64] L. Guo, E. Cui, H. Li, C.-H. Tung, Y. Wang, Singlet oxygen- and hole-mediated selective oxidation of arylethylenes to aryltetralones by Ag/Ag<sub>3</sub>PO<sub>4</sub> under visible light irradiation, *ACS Sustain. Chem. Eng.* 9 (2021) 16670–16677.
- [65] Y. Qian, D. Li, Y. Han, H.L. Jiang, Photocatalytic molecular oxygen activation by regulating excitonic effects in covalent organic frameworks, *J. Am. Chem. Soc.* 142 (2020) 20763–20771.
- [66] Y. Nosaka, A.Y. Nosaka, Generation and detection of reactive oxygen species in photocatalysis, *Chem. Rev.* 117 (2017) 11302–11336.
- [67] Y. Bu, H. Li, W. Yu, Y. Pan, L. Li, Y. Wang, L. Pu, J. Ding, G. Gao, B. Pan, Peroxydisulfate activation and singlet oxygen generation by oxygen vacancy for degradation of contaminants, *Environ. Sci. Technol.* 55 (2021) 2110–2120.
- [68] T. Xiong, Q. Li, J. Liao, Y. Zhang, W. Zhu, Highly enhanced adsorption performance to uranium(VI) by facile synthesized hydroxyapatite aerogel, *J. Hazard. Mater.* 423 (2022), 127184.
- [69] Y. Wang, G. Chen, H. Weng, L. Wang, J. Chen, S. Cheng, P. Zhang, M. Wang, X. Ge, H. Chen, W. Huang, M. Lin, Carbon-doped boron nitride nanosheets with adjustable band structure for efficient photocatalytic U(VI) reduction under visible light, *Chem. Eng. J.* 410 (2021), 128280.
- [70] K. Yu, L. Tang, X. Cao, Z. Guo, Y. Zhang, N. Li, C. Dong, X. Gong, T. Chen, R. He, W. Zhu, Semiconducting metal–organic frameworks decorated with spatially separated dual cocatalysts for efficient uranium(VI) photoreduction, *Adv. Funct. Mater.* 32 (2022) 2200315.
- [71] J. Wang, Y. Wang, W. Wang, Z. Ding, R. Geng, P. Li, D. Pan, J. Liang, H. Qin, Q. Fan, Tunable mesoporous g-C<sub>3</sub>N<sub>4</sub> nanosheets as a metal-free catalyst for enhanced visible-light-driven photocatalytic reduction of U(VI), *Chem. Eng. J.* 383 (2020), 123193.
- [72] Z. Zhang, Z. Li, Z. Dong, F. Yu, Y. Wang, Y. Wang, X. Cao, Y. Liu, Y. Liu, Synergy of photocatalytic reduction and adsorption for boosting uranium removal with PMo12/UiO-66 heterojunction, *Chin. Chem. Lett.* 33 (2022) 3577–3580.
- [73] H. Wan, Y. Li, M. Wang, Q. Zhao, Y. Fu, Y. Chen, P. He, L. Wu, Q. Meng, T. Ma, J. Yang, T. Duan, Boosting efficient U(VI) immobilization via synergistic Schottky heterojunction and hierarchical atomic-level injected engineering, *Chem. Eng. J.* 430 (2022), 133139.
- [74] W.R. Cui, F.F. Li, R.H. Xu, C.R. Zhang, X.R. Chen, R.H. Yan, R.P. Liang, J.D. Qiu, Regenerable covalent organic frameworks for photo-enhanced uranium adsorption from seawater, *Angew. Chem. Int. Ed. Engl.* 59 (2020) 17684–17690.
- [75] C.R. Zhang, W.R. Cui, W. Jiang, F.F. Li, Y.D. Wu, R.P. Liang, J.D. Qiu, Simultaneous sensitive detection and rapid adsorption of UO<sub>2</sub><sup>2+</sup> based on a post-modified sp<sup>2</sup> carbon-conjugated covalent organic framework, *Environ. Sci. Nano* 7 (2020) 842–850.
- [76] Y.K. Kim, S. Lee, J. Ryu, H. Park, Solar conversion of seawater uranium (VI) using TiO<sub>2</sub> electrodes, *Appl. Catal. B Environ.* 163 (2015) 584–590.
- [77] S. Lee, U. Kang, G. Piao, S. Kim, D.S. Han, H. Park, Homogeneous photoconversion of seawater uranium using copper and iron mixed-oxide semiconductor electrodes, *Appl. Catal. B Environ.* 207 (2017) 35–41.